CHALMERS
UNIVERSITY OF TECHNOLOGY

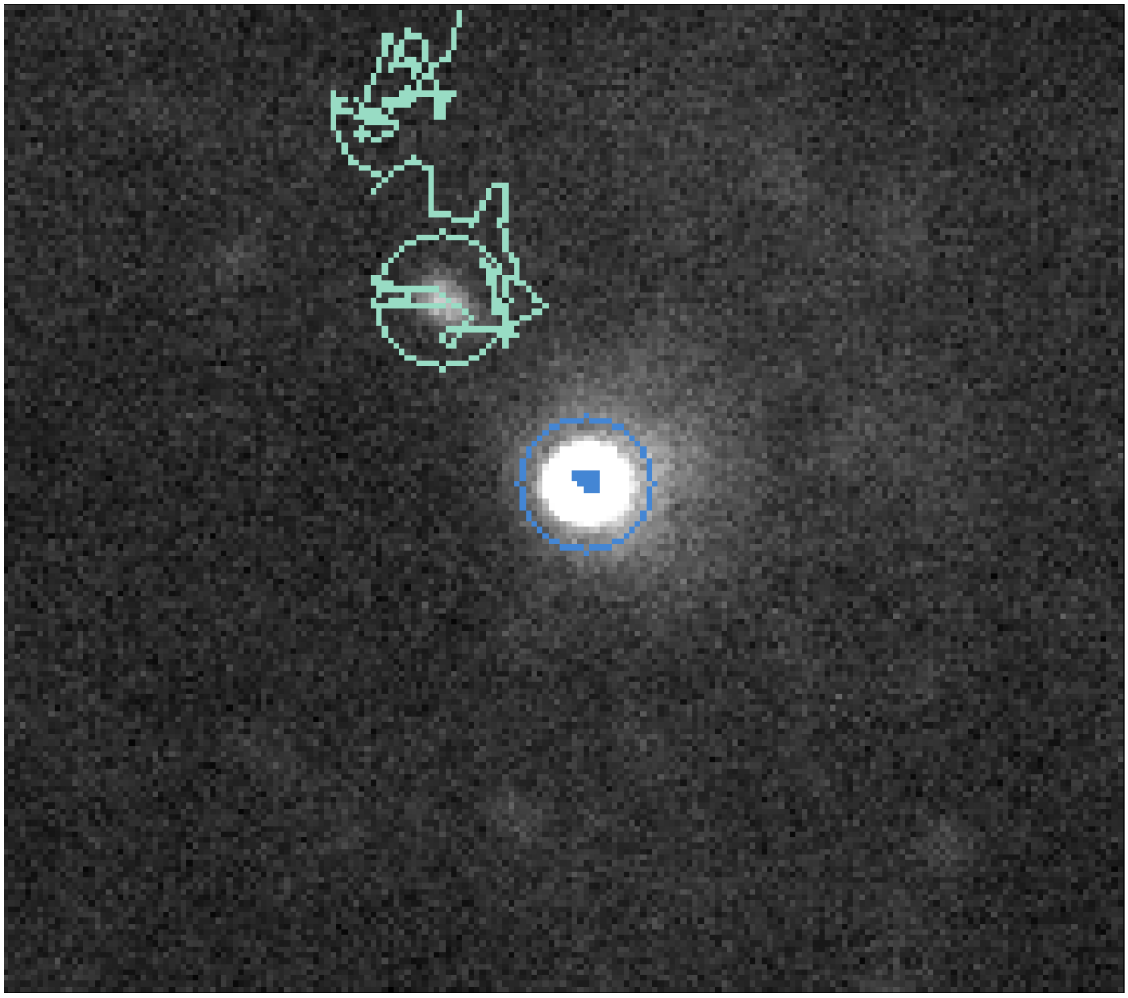

Investigations of Flow and Particle Clustering Around Optically Trapped Rotating Nanorods

Master Thesis in Applied Physics

NIELS GIESSELMANN

Department of Physics
CHALMERS UNIVERSITY OF TECHNOLOGY
Gothenburg, Sweden 2020

Master thesis 2020

Investigations of Flow and Particle Clustering Around Optically Trapped Rotating Nanorods

NIELS GIESSELMANN

CHALMERS
UNIVERSITY OF TECHNOLOGY

Department of Physics
Division of Nano- and Biophysics
Bionanophotonics Group
Chalmers University of Technology
Gothenburg, Sweden 2020

Investigations of Flow and Particle Clustering Around Optically Trapped Rotating Nanorods
NIELS GIESSELMANN

Supervisor: Hana Jungová, Department of Physics
Examiner: Mikael Käll, Department of Physics

Master's Thesis 2020
Department of Physics
Division of Nano- and Biophysics
Bionanophotonics Group
Chalmers University of Technology
SE-412 96 Gothenburg
Telephone +46 31 772 1000

Cover: Tracked trajectory of a fluorescent particle around a cluster, formed around an optically trapped, rotating nanorod

Typeset in LaTeX
Printed by Chalmers Reproservice
Gothenburg, Sweden 2020

Investigations of Flow and Particle Clustering Around Optically Trapped Rotating Nanorods

NIELS GIESSELMANN
Department of Physics
Chalmers University of Technology

Abstract

The investigation and development of nanomachines is a topic that is widely researched, as it promises applications in fields like physics, biology or medicine. A recent development of this research are light-driven rotary motors, consisting of optically trapped gold nanorods. These rods are brought to rotate by the use of circularly polarized light, making use of their plasmonic characteristics. It is now of interest to better understand the effect that these nanorotors have on their environment. In this context, this work explores the clustering of fluorescent nanospheres around an optically trapped, rotating nanorod by the means of a combination of dark-field and fluorescence microscopy. The work also discusses an attempt to track particles in order to map the microfluidic flow around the trapped nanorod. By observing the changes in brightness that occur when a particle enters this cluster, it was possible to show that the rotation of a nanorod can induce and amplify the clustering of these particles around it. Furthermore, the results suggest that higher laser powers also support stronger clustering.

Keywords: optical trap, LSPR, fluorescence, particle tracking, nanophotonics, nanorod, nanorotor.

Acknowledgements

I want to thank the whole Bionanophotonics group for their help during the process of this project, especially Mikael for giving me the opportunity to work in the group and for his patience, especially during the last weeks. I also want to thank Hana especially for her guidance and time, whenever I needed help, as well as Johanna for keeping my spirits up when I got too stressed out.

Niels Giesselmann, Gothenburg, September 2020

Contents

List of Figures

List of Tables

1

Introduction

The Master thesis at hand will take a look at optically trapped, rotating nanorods, more precisely the influence they have on their surrounding medium and other particles dispensed in it. In order to achieve this, a variety of techniques, prevalent in numerable fields of science, will be employed.

The first of these is optical trapping. It emerged in the 1970s and 80s through works of Arthur Ashkin, who accelerated and trapped micrometer-sized, dielectric particles, using the radiation pressure of a focused laser beam [1–3]. The technique is based on the property of photons to carry momentum, which can then be transferred onto objects, thereby being able to exert force and propel them. This is called radiation pressure. After being theorized by Johannes Kepler in the 17th century, this was first experimentally confirmed by Lebedev in 1901 [4] and Nichols and Hull in 1903 [5]. Since its emergence, the technique was refined is such a way that it is now possible to trap particles from a range of sizes, ranging from single atoms to biological cells [6] and is therefore applied in a variety of fields like biology and biophysics [7], chemistry [8] and, most relevant in the scope of this thesis, nanoscience [6, 9, 10].

In the latter, recent years have shown a great development regarding the trapping of metallic nanoparticles. Here, it was made use of the plasmonic characteristics of these materials in order to enhance trap stiffness and stability [6]. Plasmons are quasi-particles, that describe charge-carrier oscillations in metallic structures. As they can get excited by absorbing light, this can be used to enhance light-matter interaction [11], which creates the basis of optical trapping. In particular, it was achieved to rotate trapped gold and silver nanorods, reaching rotation freqencies in the kHz regime [12]. Here, the nanorods were trapped in 2D against a glass surface and the rotation was induced using circularly polarized light which in turn transfers angular momentum to the particle via absorption and scattering [13, 14]. While absorption had been known to be the main contributor to the rotation of spherical particles, Lee et al. showed that scattering has a bigger impact for optically anisotropic particles [13]. This lead to the development of the rotary nanomotors, mentioned above.

It is now of interest to further investigate the effects and possible applications that these nanomotors yield. Specifically, we want to observe movement of the fluid around the nanorotor. In order to do this, we will attempt to track fluorescent tracer particles and in this way map out the flow around an optically trapped, rotating gold nanorod. Early in the project, we found that these particles then tend to cluster around the trapped nanorod. While this effect hinders the initial effort on measuring the flow around the rod, it could contribute to the expanding field of nanoparticle structuring and self-assembly [15–17]. Therefore, the focus of the project shifted more to the investigation of this clustering effect.

In order to quantify this, we will measure the change in the average brightness in the area around the nanorod, thereby giving us a method to get numerical information on the growth of the cluster. We will vary the polarization state of the light in order to investigate the difference in the particle clustering behaviour between rotating and non-rotating nanomotors. We will furthermore take a look at the influence of the laser power on this issue.

2

Theoretical Background

This section aims to elaborate the underlying theoretical fundamentals of the project to the reader. It will hereby first touch on the technique of optical tweezing, as well as the plasmonic effects in metallic nanoparticles and how these can be used in combination with the former. This will be touched rather briefly. For more detailed explanations on these subjects, the interested reader can refer to [18] and reviews by Woerdemann et al [19], Bradac [20] and Urban et al [21]. For more information on the techniques and history of optical manipulation and tweezing and books by Maier [22], as well as Enoch and Bonod [23] on the plasmonic characteristics of and effects in metallic nanoparticles. These publications also serve as the major sources for these sections. We willa also take a look at how to determine the diffusivity of particles in a fluid, which was done in this study to assess the particle tracking method.

2.1 Light-Matter Interactions of Plasmonic Particles

In metals, the valence electrons can not be attributed to a single atom, but instead resemble a gas that takes up the space between the nodes of the atomic lattice. This state is called a Fermi gas [24]. By displacing the electrons in the lattice, electromagnetic waves can now excite this electron gas to oscillate. This oscillation corresponds to a quasi-particle, called a plasmon. Plasma oscillations can occur in a bulk or at the surface, depending on the characteristics of the exciting electromagnetic wave. In our case of a particle smaller than the wavelength, we can disregard the bulk properties and treat the occurring oscillations as surface plasmons. An illustration of such a plasmon can be seen in Figure 2.1. The energy transfer between the light and the plasmon is maximized if the frequency of the light corresponds to the resonance frequency of the plasmon, which can be seen as a peak in the absorption spectrum [25]. In case this is achieved, one talks about Surface Plasmon Resonance (SPR). Due to its high sensitivity towards different wavelengths and particle geometries, SPR is used and researched in a wide variety of fields like medicine, biology, chemistry or materials science [26–29].

2.1.1 Localized Surface Plasmon Resonance

Plasmons can be classified into two different groups: Localized plasmons, which are stationary and do not propagate through the material and propagating plasmons, which do propagate through the material. This kind of plasmons is observable in nanoparticles, the dimensions of which are smaller than the incident light's wavelength [22]. As mentioned above, this kind of particle is the subject of this work. The frequency of localized Surface Plasmon Resonance (LSPR) modes depends on several features, namely the geometry, composition and optical environment of the particle [30]. Since rods, such as used in this project, are non-isotropic and instead have two different axes, their LSPR spectrum will show two seperate LSPR frequencies, each one corresponding to oscillations along one of the two axes [31]. By using the LSPR characteristics of the particle, one can maximize the light-matter interaction and therefore create stable traps for plasmonic nanoparticles, even if the ray optics model discussed in 2.2 does not apply [20].

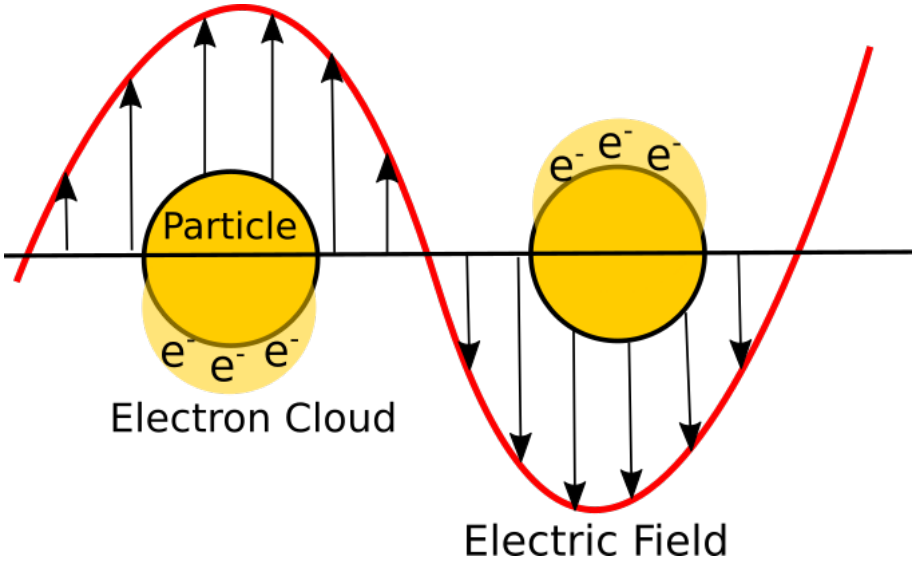

Figure 2.1: A sketch of a localized surface plasmon, showing the displacement of electrons in a plasmonic particles by an electric field.

2.2 Optical Tweezing

2.2.1 Fundamentals of Optical Trapping

Optical trapping is done using the transfer of momentum from light to the particle. A trapped particle is subject to a gradient force, as well as a scattering force. The gradient force is enacted by the shape of the beam. In the case of a Gaussian beam, the gradient force is of such shape, that the particle gets pushed into the region

with the highest intensity. This arises as the light induces a polarization inside the particle, therefore creating a dipole because of which it experiences a net force pushing it into the center of the beam, since the intensity is highest there. [32]. The gradient force can be understood more intuitively in terms of ray optics. One can imagine the beam as singular rays with varying intensities depending on the geometry of the beam and their position in it. When a ray now reaches the particle, it will get refracted, thereby transferring momentum onto the particle. If we assume a particle with a higher refraction index than the surrounding medium, the ray will be refracted away from the beam axis and the resulting force will be directed partly in the incidence direction of the light and towards the beam axis. As the higher intensity can be understood as a higher density in rays, this resulting force is larger closer to the beam axis and therefore the particle is pushed towards the center of the beam. An illustration of this can be seen in Figure 2.2: when the light gets refracted at the surface of the particle, it will experience a change in momentum, resulting in a force F_P^{in} on the particle, directed towards the beam axis. The same process happens on the way out of the particle, where the particle experiences a force F_P^{out}. The particle furthermore experiences forces from the radiation pressure of the beam, which is directed orthogonal to the particle's surface (F_R^{in} and F_R^{out}). From the illustration, one can see that the forces are mirrored on the opposite side of the particle. F_a and F_b show the total net force on each side of the particle. As, due to the Gaussian profile of the beam, the light has a higher intensity at the beam center, the forces will be stronger on that side of the particle, resulting in a net force directed towards the beam center. When the particle is locate din the center, the horizontal components of f_a and F_b will cancel each other out.

2.2.2 Optical Trapping of Plasmonic Particles

The plasmonic particles in this project are smaller than the wavelength of the trapping laser. In this case, the ray optics model described in 2.2.1 can not be applied.

To explain the process that takes place here, we will start with quantities, that can be experimentally determined, namely the scattering and absorption cross sections of a particle

$$\sigma_{scat} = \frac{k^4}{6\pi}|\alpha(\omega)|^2 \tag{2.1}$$

$$\sigma_{abs} = k\alpha''(\omega) \tag{2.2}$$

where $k = 2\pi n/\lambda$ is the wave vector of the incoming light with the dielectric constant of the surrounding medium ϵ and the wavelength λ. $\alpha(\omega)$ is the complex polarizability of the particle, which is composed of a dispersive (α') and a dissipative part

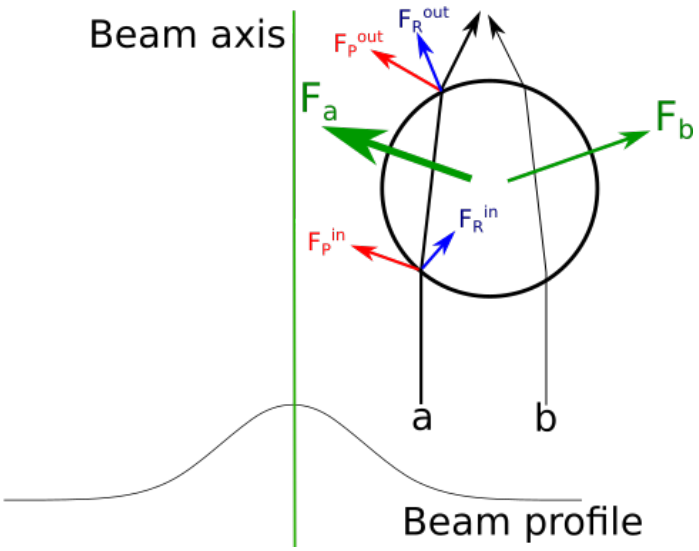

Figure 2.2: Illustration of a an optical trapping process in the ray optics regime. a and b refer to two light rays at opposite sides of the particle. F_P^{in} and F_P^{out} refer to the forces on the particle, resulting from the diffraction of the light rays. F_R^{in} and F_R^{out} to those resukting from radiation pressure. F_a and F_b are the net forces on eitehr side of the particle. The forces on the particle add up to a net force towards the beam axis, where the particle reaches equilibrium and is trapped.

(α"):

$$\alpha(\omega) = \alpha'(\omega) + i\alpha''(\omega) \quad . \tag{2.3}$$

Assuming dipolar particles with dimensions in the range of the light's wavelength, one can then use the nonrelativistic Lorentz force [33], which will lead to two forces F_{grad} and F_{scat}, behaving as

$$\langle \vec{F}_{grad} \rangle = \frac{1}{4}\epsilon_0 \epsilon \alpha'(\omega) \nabla(\vec{E} * \vec{E}) \qquad \texttt{and} \tag{2.4}$$

$$\langle \vec{F}_{scat} \rangle = \frac{1}{2}\epsilon_0 \epsilon \alpha''(\omega)\, \mathrm{Im}\left(\sum_l (E_l^* \nabla E_l\right) \qquad , \tag{2.5}$$

where ϵ denotes the dielectric constant of the surrounding medium, ϵ_0 the permittivity of free space, $\vec{E}$ the electric field of the light and l goes over the three spatial coordinates x, y and z. E_l^* refers to the complex conjugate of the electric field vector component.

We can see that the gradient force is proportional to α' and the scattering force to α''. The gradient force will lead the particle towards the spot with maximum light intensity, i.e. the center of a Gaussian beam, while the scattering force pushes the particle in the direction of the Poynting vector of the light beam.

2.3 Optical Properties and Spinning of Gold Nanorods

There are several effects which can induce rotation in nanoplasmonic particles that are trapped as explained in 2.2.2 [34].

Spherical and nonspherical particles can be rotated due to the transfer of angular momentum from the light to the particle due to absorption [35–37]. In order for this to take effect, the incoming photons have to carry a spin angular momentum, which is then transferred to the particle on absorption, making it rotate. However, optically anisotropic particles, such as nanorods, show different optical properties, which can then in turn yield different optical effects.

One part of this issue is that, due to their anisotropic geometry, gold nanorods allow for electric polarizability: An incoming electromagnetic wave displaces the electrons in the particle according to its polarization, creating an electric dipole $\vec{p}$, according to the particle's polarizability. This can be expressed by a dipole moment

$$\vec{p} = n^2 \alpha \vec{E}_1 \tag{2.6}$$

where n is the refraction index of the surrounding medium, α the particle's polarizability, which depends on its geometry and material properties, and $\vec{E}_1$ the light's initial electric field. As the field changes with time, this dipole is then accelerated by the changing field, inducing an optical torque $\vec{M}$ on the particle [34, 38, 39], following

$$\vec{M} = \vec{p} \times \vec{E}_2 \tag{2.7}$$

where $\vec{E}_2$ is the light's electric field after changing the orientation of the polarization. This mechanism can be achieved by a rotating linear polarization or circular polarization of the light [14].

In recent years, it has now been shown, that optically anisotropic particles also respond to the scattering of light. In this case, the polarization before and after scattering are not the same, meaning that an angular momentum transfer must have taken place during the scattering process [13]. In the case of gold nanorods, the scattered light has almost linear polarization, indicating a strong angular momentum transfer between the light and the particle [14]. This property is also used to experimentally determine the rotation frequency of the nanorod, discussed in Section 3.2.2.

It is to note here, that effects based on both absorption and scattering are present for gold nanorods. To quantify their contribution, the total angular momentum $\vec{M}$ can be disected into components relating to either of the effects:

$$\vec{M} = \vec{M}_{abs} + \vec{M}_{scat} \tag{2.8}$$

The absorption component can then be calculated as

$$\vec{M}_{abs} = \frac{\sigma_{abs} I_{inc}}{\omega} m\hat{z}\,. \tag{2.9}$$

In this equation, σ_{abs} denotes the absorption cross section, which relates to the ratio of the absorbed power and the incident intensity I_{inc}. ω is the frequency of the incoming light and m stands for the azimuthal order, depending on the rotational mode of the field. This can then be subtracted from the total angular momentum, which can be calculated using the Maxwell Stress Tensor, to obtain M_{scat}. This way the contribution of the scattering component can be computed, which was shown to be able to be the main contributor to the angular momentum transferred to a particle in many cases. Both of these effects are stronger with higher laser intensity, meaning that a higher laser power relates to a faster rotation [13, 40].

2.4 Diffusion of Particles in Water

Particles in water perform stochastic movement through the medium due to collisions with water molecules. We will assume this diffusion of the particle to be two-dimensional, as we can only record the particles in the focal plane of the microscope, meaning that if a movement in vertical direction occurs, the particle will just disappear from view so that no diffusion in this dimension is recorded. Following the Stokes-Einstein equation [41], the 2D Brownian diffusion coefficient of a particle in a fluid can be described as

$$D = \frac{k_B T}{3\pi\nu r}, \tag{2.10}$$

where k_B is the Boltzmann constant, T the temperature, ν the viscosity of the solution and r the particle radius. The experimental value can be calculated using

$$D = \frac{\overline{(x,y)}^2}{4t}, \tag{2.11}$$

where t denotes the time between two recorded frames and

$$\overline{(x,y)}^2 = \frac{\sum_{i=1}^{N} \Delta x_i^2 + \Delta y_i^2}{N}.$$

If a particle in a fluid is close to a surface, this surface also influences the diffusivity. According to Lorentz [42], this relationship follows as

$$D = D_0 \left(1 - \frac{9R}{16h}\right) \tag{2.12}$$

where h is the distance from the glass surface, R is the hydrodynamic particle radius, i.e. approximately the particle radius, D the measured diffusivity and D_0 the theoretical diffusivity value without any surface in proximity. From this we can calculate the distance to the surface h as

$$h = \frac{9R}{16} \left(1 - \frac{D}{D_0}\right)^{-1}. \tag{2.13}$$

It is to note that we only take a look at the 2D diffusion, as we only have access to one horizontal plane (the focal plane) in one measurement. While there are techniques now to estimate the 3D movement even in this case [43], this was not done, as this measurement was only seen as a rough estimate of the precision of the tracking software. For the same reason, surface effects in z-direction were also disregarded in the scope of this investigation.

3

Experimental and Analytical Methods

3.1 Experimental Methods

3.1.1 Experimental Setup

In this work, we used a setup consisting of of an inverted microscope using dark-field illumination, which was used in previous works [40]. We modified the setup by adding the option of using fluorescence microscopy instead of dark-field to aid the visualization of fluorescent tracer particles.
For trapping a *Toptica XTRA II* laser is used, emitting light with a wavelength of 785 nm. The beam is circularly polarized by the use of a quarter-wave plate that gets preceded by a half-wave plate. While the quarter-wave plate achieves circular polarization, this circularity is disturbed by other parts of the setup, in such a way that the light that arrives at the sample is elliptically polarized. The half-wave plate has the purpose of reversing this effect by creating elliptically polarized light in combination with the quarter-wave plate in such a way that the light at the sample is circularly polarized. The quarter-wave plate can also be removed from the setup in order to use linearly polarized light.

The laser is then focused close to the upper surface of the sample cell, trapping the rod there. The upper surface serves hereby as a boundary of the trap. This needs to be taken into account when analyzing microfluidic effects, since the surface has an effect on these. The rods are gold nanorods, which measure about 140 nm along their long axis and 70 nm along the short axis.

For the excitation of the tracer particles, an *Energetiq EQ- 99 XFC* laser driven light source is used. Its light is filtered for 580 nm and then fed into the sample cell via several mirrors. It is hereby focused roughly on the back focal plane, meaning that it is relatively broad when reaching the sample (in the range of several μm). The particles that are used are *ThermoFisher FluoSpheres™ Carboxylate-Modified*

Microspheres, with a diameter of 200 nm. The stock solution encompasses 2 % solids and they absorb light of a wavelength of 580 nm while emitting 605 nm. By the use of an emission filter, this light gets isolated before reaching the camera. This way, the light from the rod becomes negligible compared to the emission from the fluorescent particles, allowing an analysis of their behaviour without interfering light from the rod. It is to note that these microspheres are considerably larger than the rod, which could lead to flows not being recognized due to their inertia. However, it was not possible to use smaller spheres, as the camera did not show enough sensitivity to record these at a reasonable frame rate (≈30 Hz).

As mentioned above, the visualization can be done in either dark field or fluorescence microscopy. Generally, dark field was used for the trapping process, as it shows both rods and tracer particles. Fluorescence was then used to visualize the clustering process, as it mostly filters out the rods and shows only the tracer particles. The image acquisition is done using a *ANDOR Neo sCMOS* camera. The acquisition of data on the rotation of the rod is done by a photomultilplier tube (PMT) that captures backscattered light from the nanorod. The rod scatters light differently depending on its orientation. This backscattered light gets reflected by a dichroic mirror that lets the trapping laser wavelength pass. An illustration of the setup can be seen in Figure 3.1.

3.1.2 Particle Selection and Sample Cell Fabrication

Gold Nanorods There are two kinds of particles that are used in the project. The gold nanorods, which get trapped and rotated and the tracer particles, that were used to map the flow of the medium surrounding the gold nanorod. The rods used in this project have dimensions of around 140 nm along their long and 70 nm along their short axis. Figure 3.2 shows a Scanning Electron Microscope picture of the nanorods (3.2b) and their extinction spectrum (3.2b). The pictures were obtained from Hana Jungová [40] who used nanorods from the same batch as in this project. The extinction spectrum describes at which wavelengths the rods absorb the most light. We can see two distinct peaks at around 550 and 760 nm. These respond to the localized plasmon resonances corresponding to the short and long axis respectively. The nanorods were chosen in such a way that their long-axis LSPR coincides with the laser wavelength used in this study (785 nm), securing an effective momentum transfer between the light and the particle.

Tracer Particles The fluorescent microspheres that are used as tracer particles in most of the project are *ThermoFisher FluoSpheres™ Carboxylate-Modified Microspheres* with a diameter of 200 nm. The stock solution encompasses 2 % solids and they absorb light of a wavelength of 580 nm while emitting at 605 nm. Figure

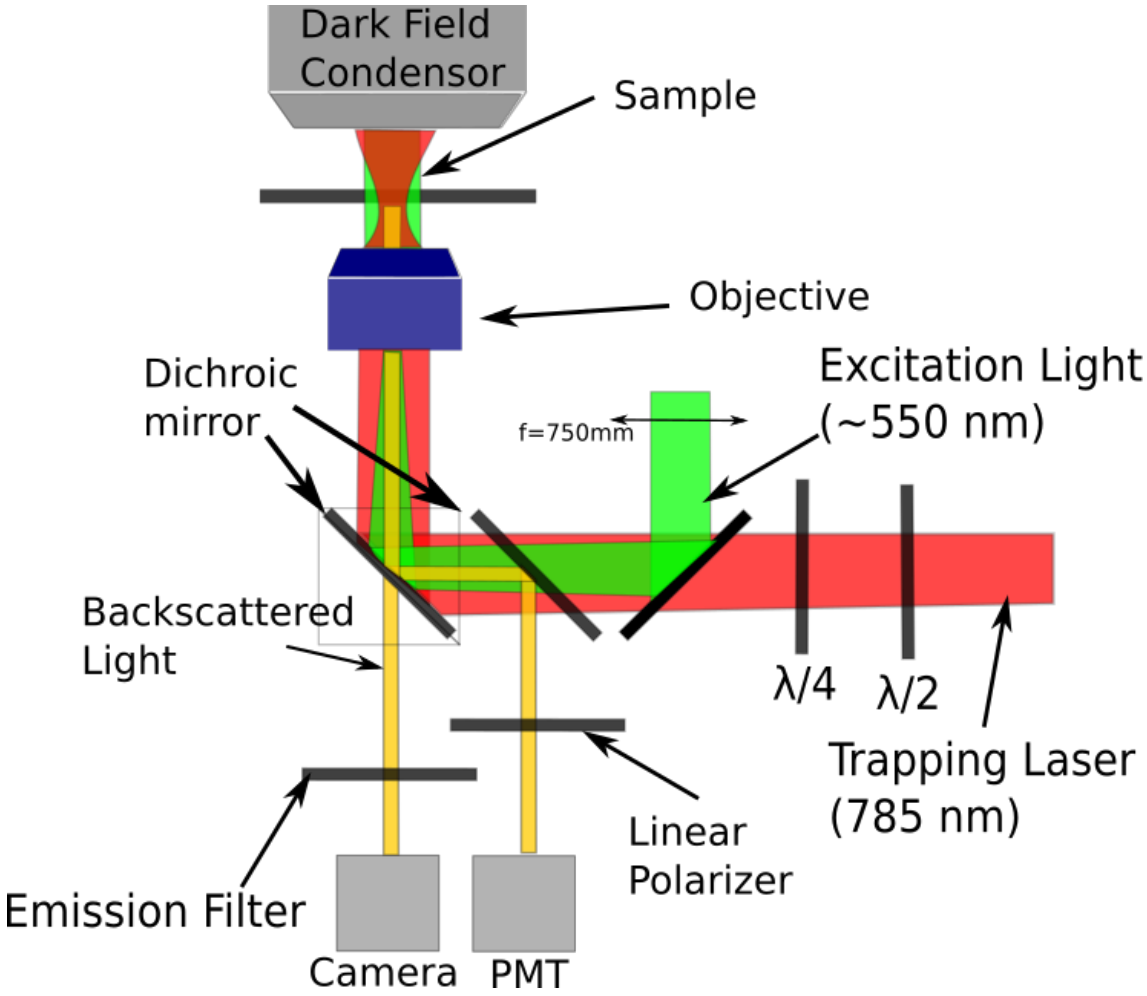

Figure 3.1: A schematic illustration of the experimental setup.

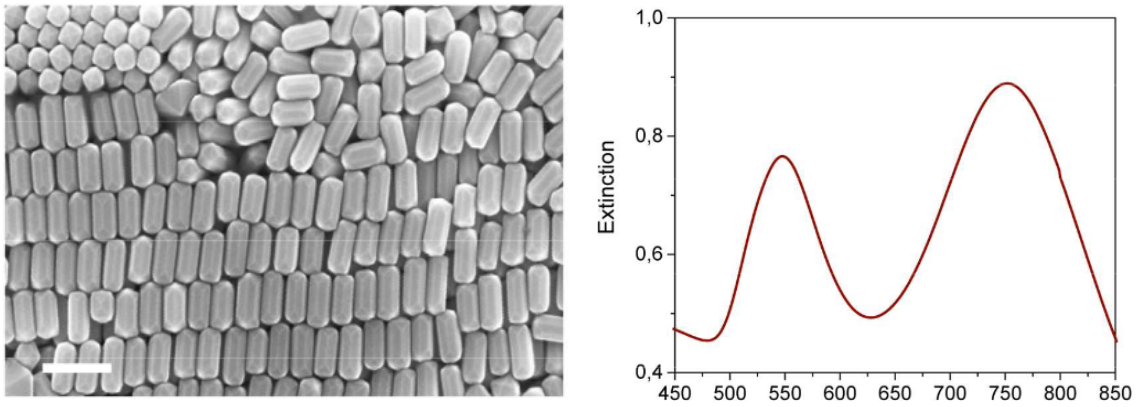

(a) **(b)**

Figure 3.2: (a) Scanning Electron Microscope picture of the used nanorods. The scale bar in the bottom left corner represents 200 nm. (b) Extinction spectrum of the nanorods. The two peaks correspond to the LSP resonances for the short and long axis [40].

3.3 shows their excitation and emission spectra, obtained from the ThermoFisher Scientific website [44]. It shows that both peaks are far from the laser wavelength, ensuring minimal influence from it on the excitation of the particles. It is to note that these particles are larger than the nanorod. This means that their size could make the flow mapping less precise.

The standard particle concentration that was used is 1:20000 for both rods and particles. Additionally, 0.1 M CTAB was added at a concentration of 1:50 to prevent random aggregation of particles.

Sample Cells and Fabrication Three different kinds of cells were tried out in the course of finding the fitting one for the project. Initially, a thicker cell made up of a microscope slide, a sticky spacing component as well as a cover glass with a thickness of around 100 μm was used. A sketch of this cell is displayed in Figure 3.4a.

To limit the movement of the tracing particles in z-direction, the fabrication of a thinner cell was attempted next. For this, a microscope slide was covered with polystyrene beads as spacers for the cell, as also described by Böhm et al [45]. Then the solution is applied, a cover glass with an area of 23×23 mm is laid over the area with spacer beads and then sealed. This cell type can be seen in Figure 3.4b.

A third cell setup was previously used by Per Rudquist [46–48] and can be seen in Figure 3.4c. This cell is similar to the first attempt on a thin cell. It consists of two pieces of microscope slides with spacer beads in between that are glued together

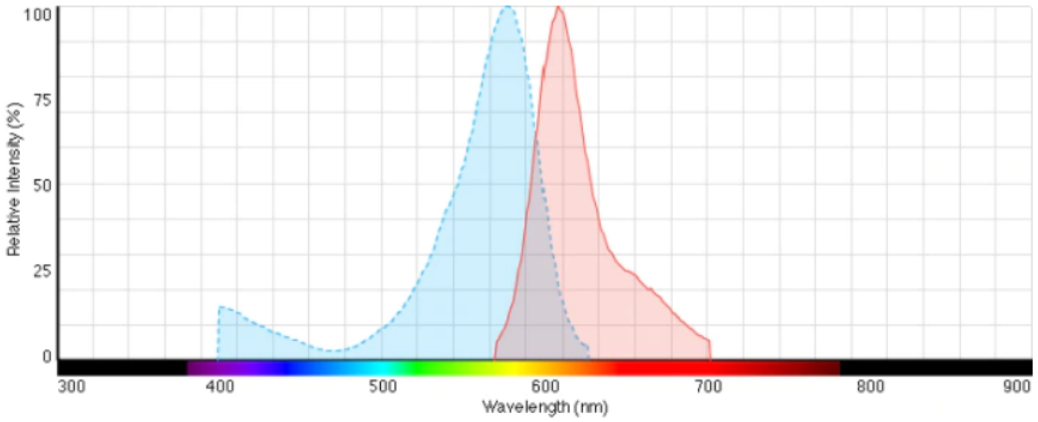

Figure 3.3: Excitation (blue) and emission (red) spectra of the fluorescent microspheres used as tracer particles. The image was obtained from the *ThermoFisher Scientific* website [44].

with UV-curable glue. Both glass slides have an area of approximately 10×10 mm. The solution can be placed next to an opening in the cell and moves inside by means of capillary forces. It can then be sealed by UV-curing glue or vaseline for example. Due to its small size it has to be placed on top of a microscope glass slide, which might influence the beam shape of the laser as well as induce scattering on the additional glass surfaces.

Of the three sample cell types described in Section 3.1.2, the first one was used for the rest of the experiments. The second cell type proved to be rather unreliable due to random flows, probably induced by the drying sealant (nail polish) in combination with the rather large area of the cover glass and its flexibility. The third cell type seemed to be the most fit for the experiment. However, due to external reasons, it was not possible to acquire these cells in sufficient quantities for the experiment that were to be conducted, which is why the choice was made to use the initial cells, even though they allow much more tracer particle movement in vertical direction.

3.1.3 Microscopy Methods

Dark-field Microscopy The fundamental principle of dark-field microscopy is to visualize particles as scattering objects in the specimen. To achieve this, the light reaches the sample from a condenser at a high angle relative to the optical axis of the setup. This is achieved by blocking the center part of the incoming light, so that light only reached the sample from the edges of the condenser. The idea is then

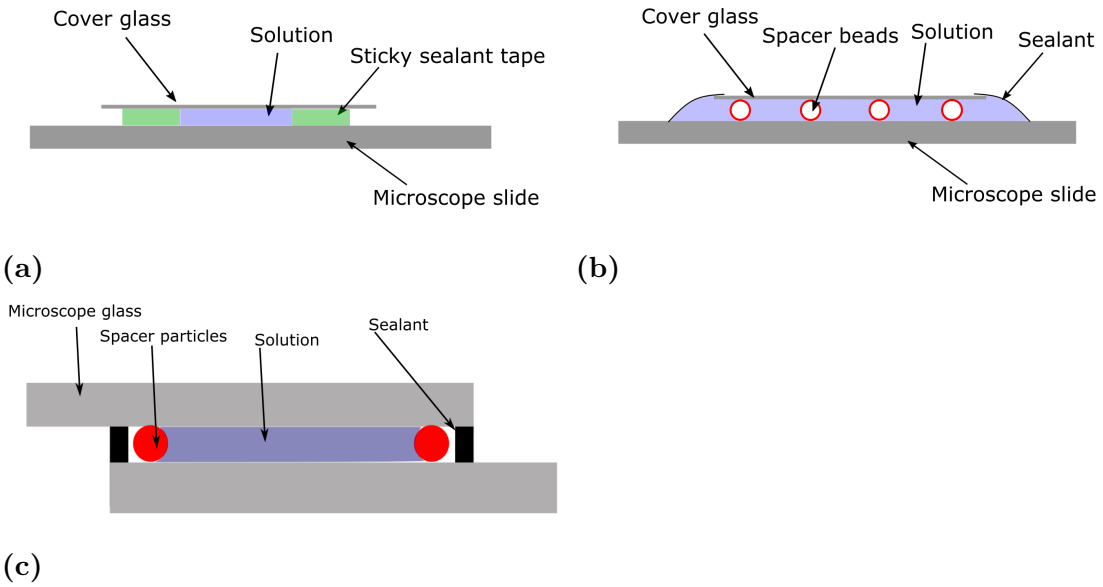

Figure 3.4: Sketches of the three cell types used so far in the project. (a) The thick cell, which has already been used before in this kind of setup [40]. A sticky spacer tape separates the microscope slide and the cover glass with a thickness of around 100 μm. The solution is applied on the microscope slide before the cover glass is stuck on. (b) A thin cell with a height depending on the diameter of the spacer beads. (c) The third cell version, obtained from Per Rudquist [46]. Two cut microscope slides are spaced with polystyrene beads and glued together with UV-curable glue.

that the particles one wants to observe scatter and refract the light in such a way that it then reaches the objective. The incidence light is hereby not collected. This way, the particles appear as bright dots before a dark background [49]. A schematic illustration of a dark-field setup can be observed in Figure 3.5.

Fluorescence Microscopy As the name suggests, fluorescence microscopy is a form of microscopy, making use of fluorescent molecules. Fluorescent molecules get excited at a certain wavelength of light, meaning that they absorb the incoming photon and thereby move to a higher energy level, where the difference of the energy levels corresponds to the energy of the incoming photon.
The molecule then relaxes and reaches the lowest excited state by non-radiative transitions, before dropping to the ground state by the emission of a photon. This way, the emitted wavelength is longer than the incident one, making it possible to filter it out and only capturing the emitted light. This way, one observes only the emitted light from the molecules, minimizing background, scattered or incident light. It is to note, that only specific molecules have these characteristics and each of those has its own absorption and emission wavelengths [50]. An illustration of

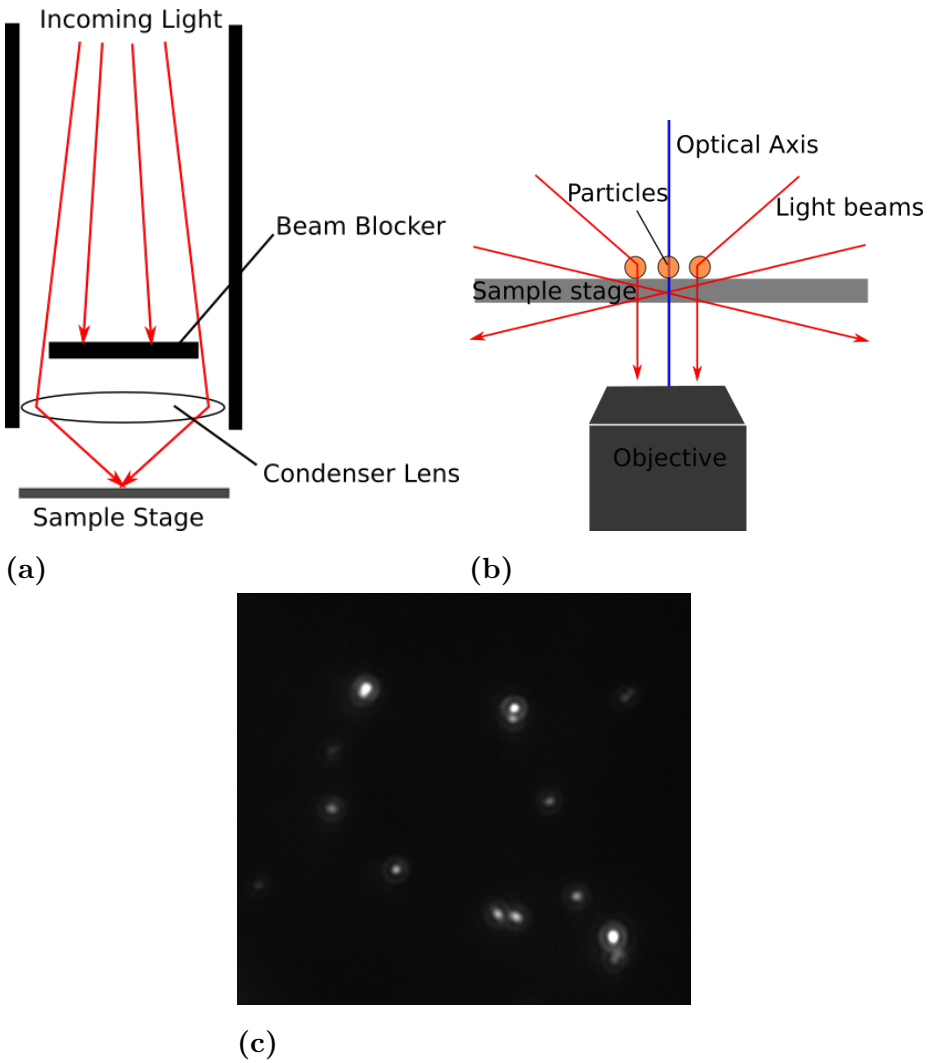

Figure 3.5: (a) Illustration of the working principle of a darkf field condenser. (b) Illustration of the scattering and imaging process in dark field microscopy. (c) An example image recorded with dark field microscopy.

the process can be seen in Figure 3.6.

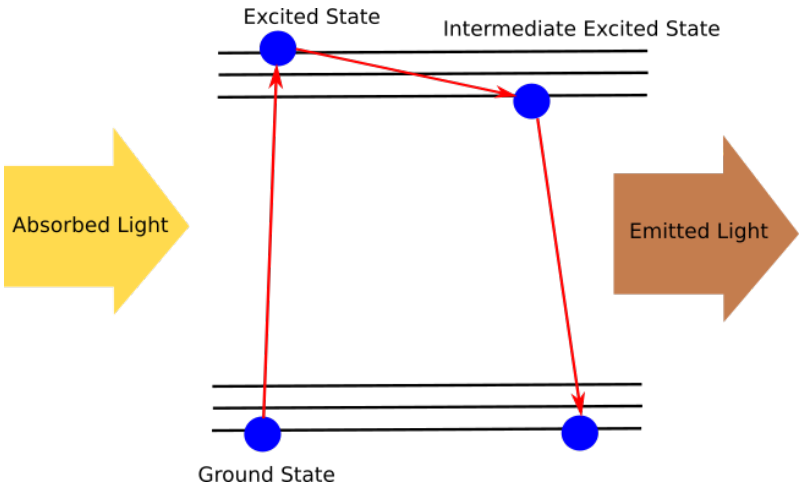

Figure 3.6: An illustration of the process made use of in fluorescence microscopy. The lower three lines represent vibrational states of the ground state and the upper ones vibrational states of the excited energy level. The molecule gets excited by an absorbed photon, then relaxes, before returning to the ground state by emission of a photon.

3.2 Analytical Methods

3.2.1 Measurement of the Laser Power

When comparing the behaviour of the cluster at different laser powers, it is of course important to measure the latter. This was done before the trapping, as one needs to replace the sample with a power meter to measure the laser power. In this study, a *ThorLabs PM100D* powermeter with a *ThorLabs S121C* photodiode power sensor was used. When measuring the power of circularly polarized light, the first step is to make sure that the polarization of the light is as circular as possible. In order to do this, a linear polarizer is placed before the powermeter. This polarizer can then be turned, so that one can compare the power measured by the powermeter for different polarizer orientations. To achieve circularity, the measured powers after the polarizer should be the same for all orientations. To measure the power itself, the polarizer is now removed, different currents can be applied to the laser and the corresponding measured laser power can be recorded.

It should be noted at this point that a momentous mistake was made in the course of this study, which was unfortunately noted too late to fix it. The laser power was measured with the linear polarizer still in place. This is not a big problem when

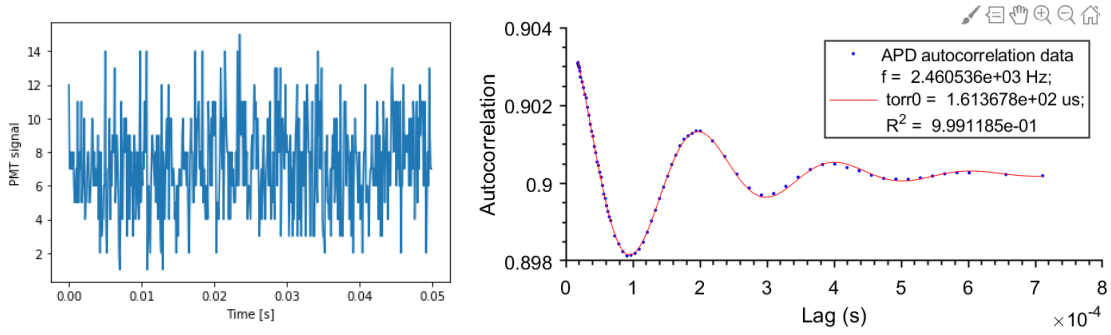

(a) **(b)**

Figure 3.7: (a) Intensity oscillation signal from the photomultiplier tube over time. (b) An example for a fitted autocorrelation curve of the scattering intensity of a nanorod rotated by circularly polarized light. torr0 denotes the autocorrelation decay time and f the average frequency of the rotation.

measuring the power of linearly polarized light, as the vast majority of the light still passes the polarizer, if it is oriented correctly. For circular polarization, however, this has the effect that half of the light does not pass the polarizer, meaning that only 50 % of the power are recorded. The consequences of this mistake will be discussed further in the relevant parts of Chapter 4.

3.2.2 Determination of the Rotation Frequency of Trapped Nanorods

A trapped nanorod will backscatter some light that is used for trapping. Due to the effects described in Section 2.3, this backscattered light will be linearly polarized, but its polarization will rotate together with the rod. This scattered light is then passed through a linear polarizer and recorded with a photomultiplier tube (PMT). As the light can only pass through the polarizer when its polarization is aligned with that of the polarizer, we will get an intensity signal that oscillates over time. An example for such a signal can be sen in Figure 3.7a. This way, we can directly connect this oscillation with the rotation of the rod, as a peak in the transmitted intensity has to relate to a certain alignment of the rod that occurs every half period [35]. An autocorrelation function is used to analyze the time dependence of the scattering intensity. This function in essence compares a signal with a copy of itself that is shifted in time. This way, repeating patterns in the signal can be found. Since the intensity of light entering the PMT depends on the orientation of the nanorod, there will be an intensity peak each half rotation time of the nanorod. The autocorrelation curve then shows how well the signals correlate for different lag times. Figure 3.7b shows an example of such a curve including a fit of the form

$$C(\tau) = I_0^2 + 0.5 I_1^2 \exp\left(\frac{-\tau}{\tau_0}\right) \cos(4\pi f) \quad , \tag{3.1}$$

where τ denotes the lag time, I_0 the average intensity, I_1 the amplitude of the intensity fluctuation, f the rotation frequency and τ_0 the decay time [40]. The quantity τ_0 can hereby be related to rotational Brownian motion: It denotes the time in which the correlation decays, meaning the correlation breaking down due to incremental shifts of the rotational phase over the time of several rotations. This decay is due to the rotational Brownian motion of the rod and is dependent on the temperature and viscosity of the surrounding medium, as well as the size and shape of a given nanorod [12]. The time between two peaks represents the period $T/2$ of a half rotation, from which the frequency can be determined as $f = T^{-1}$. The analysis of the rotation frequency was used in the study in order to make sure that a rotation actually took place. This way it is possible to compare these with non-rotating systems without having to take into account nanorods at circularly polarized light, that are not rotating. This could theoretically happen, for example when they get stuck on the glass surface.

3.2.3 Tracer Particle Tracking

At first, it was attempted to track particles diffusing around the nanorod in order to observe a potential orbital movement induced by its rotation. For this, a 2D tracking tool from the Fiji distribution of ImageJ, a platform developed for biological image analysis at the Max Planck Institute for Cell Biology and Genetics, was used [51, 52]. The algorithm of this tool is based on particle recognition in subsequent frames, based on three parameters: The particle radius, a cutoff value and the brightness percentile. The particle radius is quite self-explanatory. It describes the maximum radius in pixels that the image of a particle can have in order to be recognized as one. In the measurements that will be discussed in this thesis, this threshold was set to 8. The cutoff value has the function to filter out non-relevant signals, such as dust. Since dust particles would already be too large to be recognized on our length scales and large-scale clustering did not appear to happen in the measurements where this tool was used, this parameter was set to 0. The brightness percentile describes the brightness threshold at which signals are taken into account as potential particles.This can either be an absolute value or one relative to the background. It is described by a value between 0 and 1 and pixels with a brightness value higher than the percentile are considered. In our case, this was set to 0.9, meaning that pixels with a brightness at least 90 % higher than the background are considered as particles.

After recognizing the particles in the various frames, the next step is then to stitch

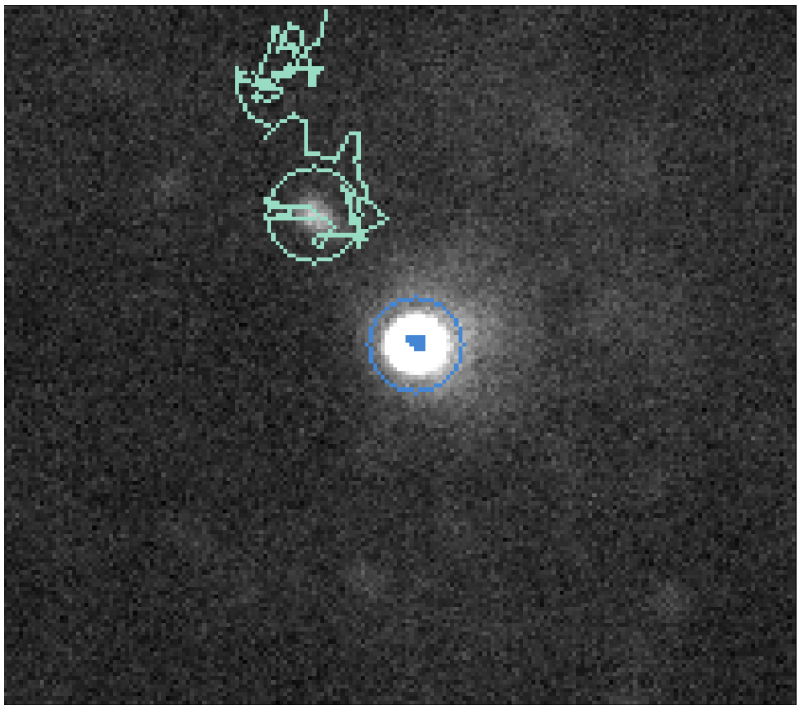

Figure 3.8: An example of a trajectory obtained by the particle tracking process. The blue-circled particle in the middle is a cluster forming around the rod.

together the trajectories of these particles. For this, one can define two more parameters, namely the link range and the displacement. The displacement describes the maximum amount of pixels that a particle between two frames that will be considered part of the same trajectory. The link range then defines the number of frames that will be taken into account to link a trajectory. In this case, a displacement of 10 px and a link range of 2 were chosen. This means that two recognized particles in to succeeding frames will only be linked if they are closer than 10 pixels from each other. Furthermore, in stitching together a trajectory, it will look two frames ahead to see if these particles belong to the same trajectory. A more detailed description of how the algorithm works can be found in [52].

Figure 3.8 shows an example trajectory from this process. There, you can also see an example of a cluster forming around the nanorod. This matter will be discussed later. The tracking process also yields numerical information on the trajectories in the form of coordinates, which can then be used for further analysis.

3.2.4 Measurement of Tracer Particle Clustering

The process of particles clustering around the nanorod was quantified by selecting a fixed region of interest (ROI) around where the nanorod is trapped. The average brightness in that region was then monitored by using the Multi Measure tool, im-

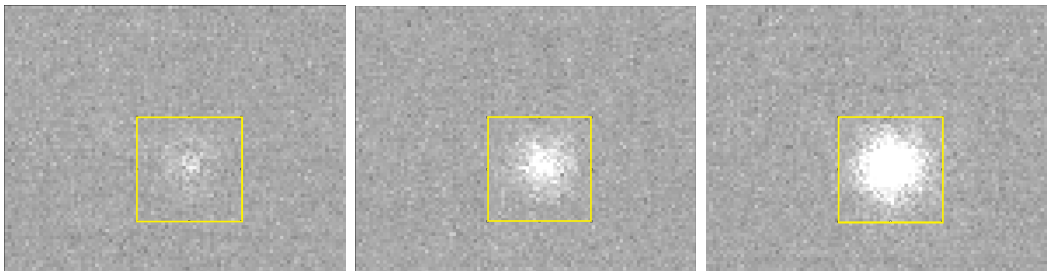

(a) after 67 s **(b)** after 164 s **(c)** after 238 s

Figure 3.9: Camera images of the region around a trapped nanorod, shown at three different times. The yellow box around it shows the region of interest in which the average brightness was measured over time.

plemented in Fiji/ImageJ, as illustrated in Figure 3.10.

When the average brightness is plotted over time, it reveals step-like increases, as can be seen in blue in Figure 3.10a. To quantify these steps, a Savitzky-Golay filter [53] is first applied to the data and the derivative of this filtered data is taken. A visualization of the filtered data compared to the original data is shown in Figure 3.10a. Then, an algorithm is applied, which sets a certain threshold value. If the gradient crosses this threshold value and then crosses back again, a step is registered. Going back to the original data, the size of the step is then simply determined by taking the difference of the values at the beginning and end of the registered step in the data, both in a certain window to compensate for noise. The position and size are then saved and can be used for further analysis. An example of this process is visualized in Figure 3.10b.

It is to note that this method encapsulates a couple of drawbacks. For one, the filtering processes has the potential to erase information from the data. It therefore has to be applied carefully and the filtered data has to be compared thoroughly with the original data to minimize this effect. The other big possibility for error is that the step threshold has to be adjusted to each dataset individually by the user, meaning that there can be problems in the comparability of the results of different datasets, as well as the threshold to be chosen rather arbitrarily. The user has to be very careful to not miss steps that can be mistaken for noise. Therefore, a quite liberal interpretation of steps was applied in order make sure that all steps are captured. This has the result that noise gets picked up as steps as well, which will be discussed in Chapter 4.

In order to assess the validation of this method, it was attempted to recreate the original data with the steps identified with the algorithm. To achieve this, the first

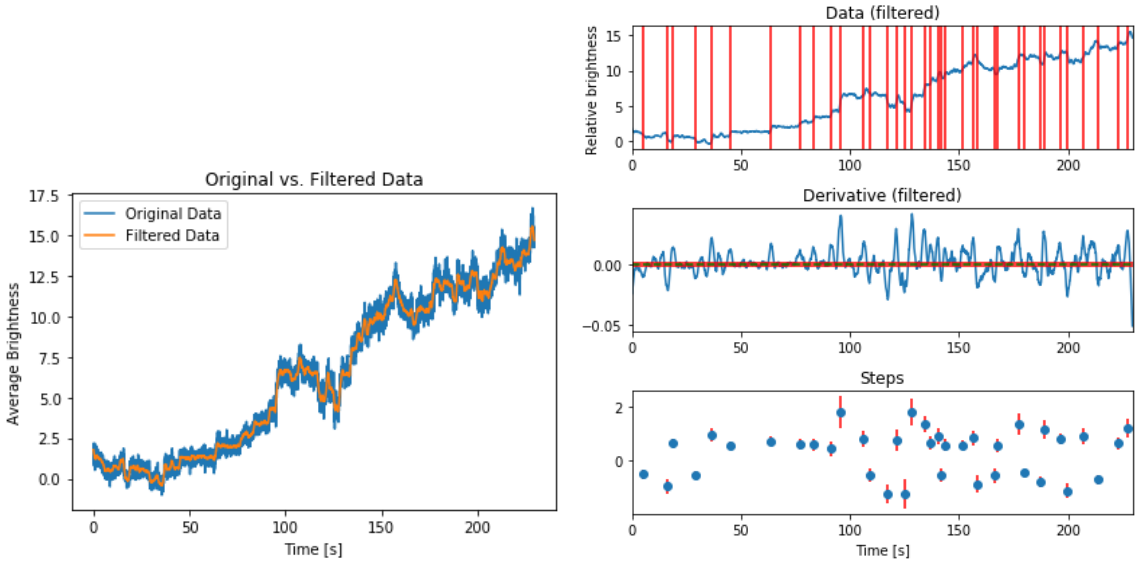

(a) **(b)**

Figure 3.10: (a) Comparison of the original data and the data after applying a Savitzky-Golay filter. (b) Top: Filtered data with marks at the locations of the registered steps. Center: Gradient of the filtered data and threshold value. The threshold value is also applied in the negative. Bottom: Scatter plot of the sizes of all registered steps against their location in time.

point of the data was taken as a start point and each time a step occurs, its step size is added to the value. Therefore, only the points where a step occurs should be looked at.

To give a rough estimate of the overall precision of the method, the last point of the recreated curve is compared to the last original data point in order to quantify the quality of the recreation. An example of this can be observed in Fig 3.11. It contains two graphs, as the step detection process was repeated once more, using only steps with a certain minimum step size in order to decrease influence from noise. This will be discussed in more detail in Section 4.4.

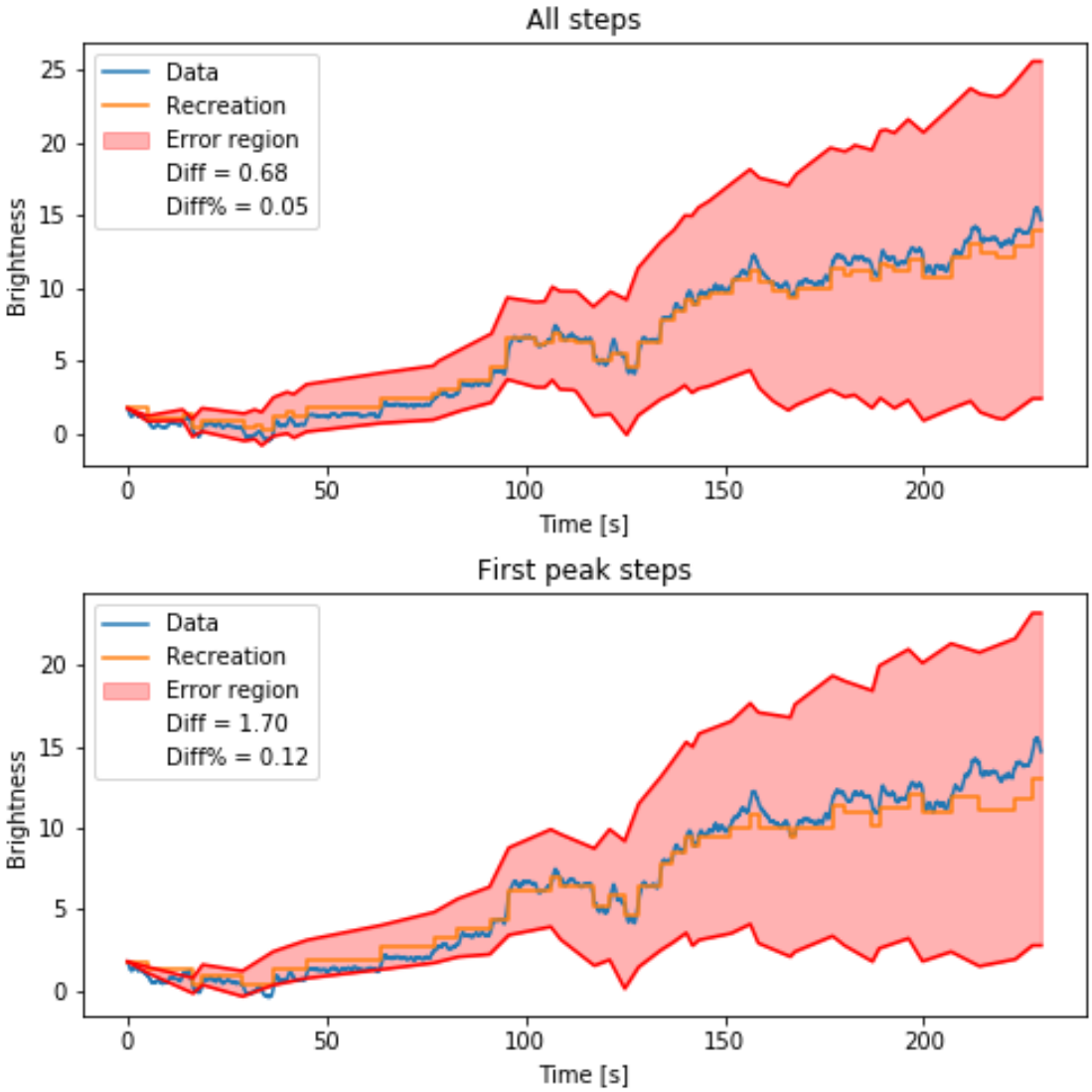

Figure 3.11: Visualization of the recreation of the curves by applying the recorded steps. The upper figure shows the curve with steps of all sizes taken into account, while the lower one only uses steps of a minimum size of 0.41. More on this in Section 4.4. The blue plots represent the original data, the orange plot the recreated curve. The red area shows is the added up error of the steps. *Diff* is the difference between the last datapoint and the last point of the recreation curve and *Diff%* refers to the ratio between said difference and the original datapoint.

4

Results

4.1 Laser Power Determination

Figure 4.1a shows the laser powers that were measured with the linear polarizer in front of the powermeter. As discussed in Section 3.2.1, this is an incorrect measurement, as approximately half of the power of circularly polarized light is lost in the polarizer. In order to correct this issue as good as time allowed, the measured values for the power of circularly polarized light (Fig 4.1a) are multiplied by a factor of two. The resulting powers can be observed in Figure 4.1b.

Since during the measurement, only the current that is applied to the laser can be influenced directly, the laser power assessment was crucial to choose the applied current in such a way that they yield reasonable laser powers. The goal was to achieve similar laser powers for linear and circular polarization. Since the values in Figure 4.1a were assumed to be the correct values, this means that the actual values are only partly comparable. Precisely, the currents that were chosen for the measurements were 1200, 1250 and 1300 mA for linear and 1300, 1400 and 1500 mA for circular polarization, since these would have lead to similar laser powers when using Fig 4.1a. However, if we take the corrected values in Fig 4.1b, this leads to an imbalance in the laser power, where only the last value at linear and the first value at circular polarization are comparable.

While this vastly decreases the security with which conclusions can be drawn from the study, we will still try to see if any trends or indications can be drawn from the results and we will put it into context with the laser power issue whenever it becomes relevant.

4.2 Diffusivity Estimation

The first thing to investigate was the diffusivity of the particles without a trapped nanorod and if the experimental data matches the theoretical values. The goal here is to assess the precision of the particle tracking algorithm and procedure. In this in-

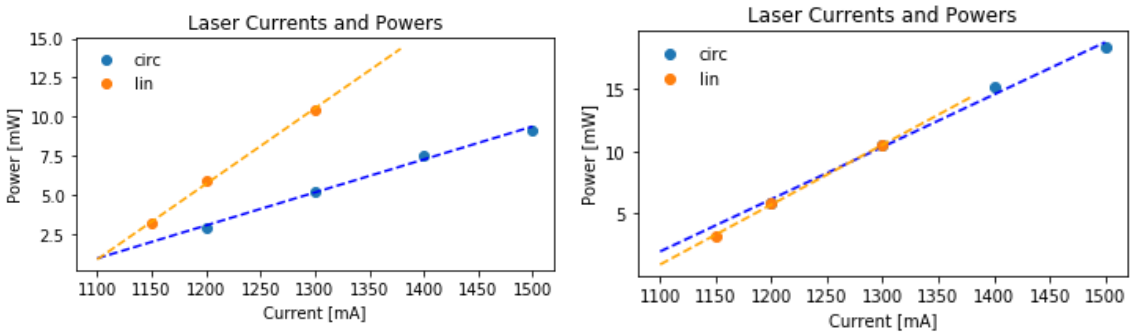

(a) **(b)**

Figure 4.1: (a) The measured laser power with the polarizer in front of the powermeter. (b) Corrected laser powers. The laser power values in this plot for circular polarization are two times those in (a).

stant, gold spheres with a radius of 100 nm were used. Furthermore, water was used as a solvent, therefore using a viscosity of ≈1 mPa·s. Considering a temperature of slightly above room temperature (about 300 K), water as solvent and the radius of the used particles of about 100 nm. Using Equation 2.10 this leads to a theoretical value of about 2.14 $\mu m^2 s^{-1}$. This value can now be compared to the experimental data. The experimental value is determined by using the mean square displacement of a particle (Equation 2.11).

After an analysis of in total 517 trajectories, a value of 2.03±1.09 $\mu m^2 s^{-1}$ was determined. One can see that the relative error here is quite large, even though the average value is quite close to the theoretical one and there are a lot of trajectories that go into the calculation. This could be explained by the variety in the various trajectories. As the length of the trajectories varies, this might impact the diffusion constant value as well, leading to a relatively precise total average value, varying about 9 % from the theoretical one at 2.14 $\mu m^2 s^{-1}$, but resulting in a large spread of individual values between the single trajectories.

It also seems like the experimentally determined value tends to be lower than the theoretical one. This could be due to the fact that only particles that are close to the upper glass surface of the cell are recorded. This could have an effect on the Brownian behaviour of the particles. Following Eq. 2.13, we get a distance from the surface of about 1.09 μm which seems fairly realistic.

4.3 Trajectory Analysis

In the next step, the trajectories of tracer particles were analyzed in order to identify a possible effect from the rod rotation. This measurement was done using dark-field microscopy and gold spheres, as well. Figure 4.2a shows all tracked trajectories in one data set. We can see that in the middle of the graph, only one trajectory is observed with blank space between it and the other trajectories. This represents the nanorod and the empty space is the area in which the brightness of the rod made it impossible to track particles. This problem was attempted to be overcome by the use of fluorescence microscopy. Unfortunately, this did not yield promising results, as the fluorescent light coming from the particles was too dim to be recorded by the camera in such a way, that particle tracking would be possible.

After capturing the trajectories, the movement of the tracer particles was analyzed in respect to their distance from the rod. This way, it was tried to create a map of the flow around the rod. The obtained plots can be observed in Figures 4.2b, 4.2c and 4.2d, showing the total, radial and azimuthal velocities of the particles, respectively, behaving as

$$v_{tot}^2 = v_{rad}^2 + v_{az}^2 \quad . \tag{4.1}$$

Fig 4.2b shows the mean velocity of the particles at a certain distance from the rod. We can see that in general, the velocity stays relatively constant at about 0.3 to $0.4\,\mu$m/s. There are however two things to observe: Firstly, we can see a larger bar at a distance of $4.0\,\mu$m from the rod. This could indicate an actual flow speed maximum, especially since the azimuthal velocity shows a maximum in this region as well. To confirm this, it would have to be compared to theoretical investigations of this matter. Unfortunately, most literature on rotating rods or cylinders deals with them rotating around the long instead of the short axis and doing an own theoretical investigation is out of the scope of this project. The second explanation would just be statistical variance. In this region, 17 particles were tracked, which is less than its adjacent values. While this should be enough to give a relative idea of the average velocity, it does probably not give enough certainty to have a clear answer to this issue and further direct investigation of this are needed. Secondly, we can see the mean total velocity decreasing between about 5.4 and $6.4\,\mu$m from the rod. It is to note though, that in this area, only few particles are observed. Therefore one should not jump to conclusions from this behaviour, as it is not statistically sound.

Figures 4.2c and 4.2d do not seem to yield any patterns that could give clues about the flow behaviour. For both, the distribution of velocities seem to be rather random. The only thing to note is that the absolute value of the radial velocity seems to

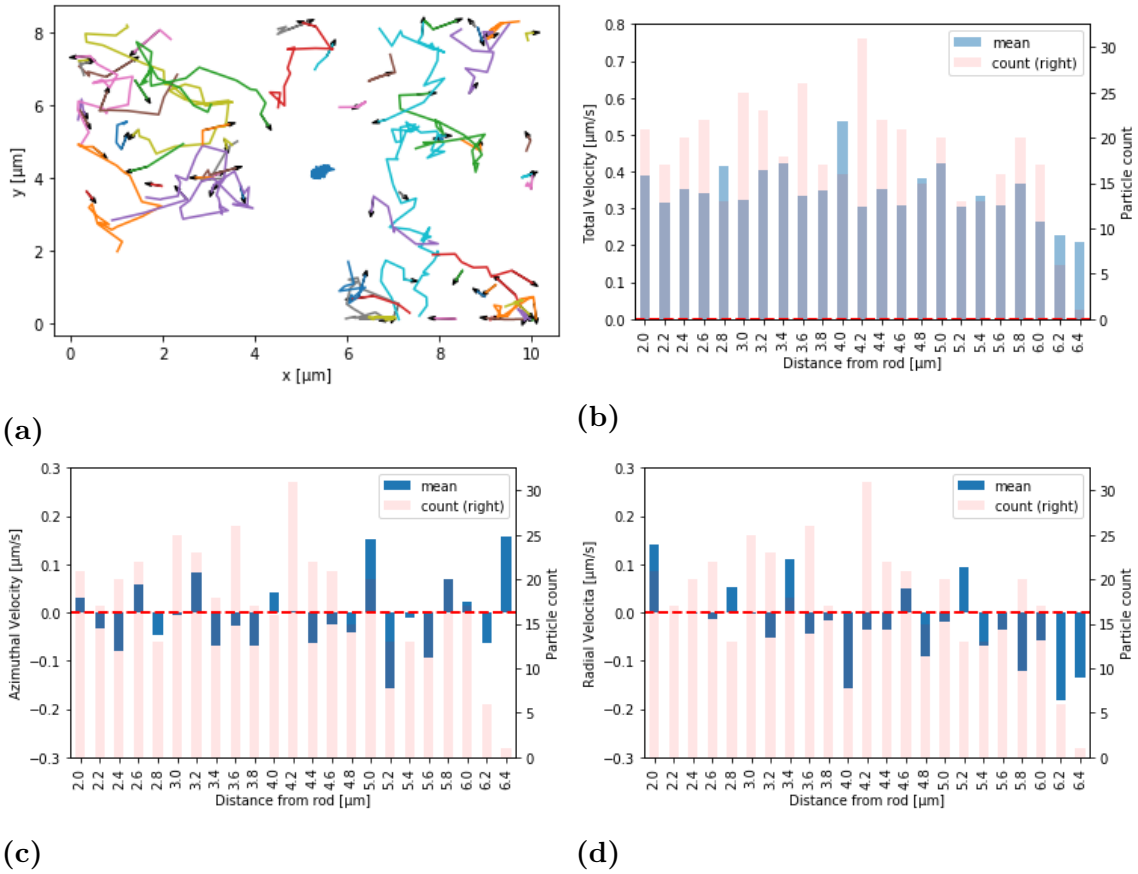

Figure 4.2: A map of all recorded trajectories in the analyzed dataset including the rod trajectory in the center with arrow heads indicating the movement direction (a), as well as bar plots of the mean total (b), azimuthal (c) and radial (d) velocities of the tracer particles around the trapped nanorod. The red bars show the amount of particles that were observed in the corresponding position, the value of which can be seen on the y-axis on the right side of the plot. The position denoted on the x-axis is the position of the particle in the initial frame before movement.

be highest at 5.0 and 5.2 μm/s, however, this does not seem to suggest any specific behaviour, as these maxima do not coincide with any outstanding values for the total or azimuthal velocities.

These results also do not correspond to expectation. Considering a rotating rod in a liquid, the expected result would have been a higher velocity closer to the rod. A reason why this was not observed could be that, as hinted upon before, the rod produces a relatively large, bright spot (about 2 μm), which could cover the area in which this behaviour possibly happens. The solution for this could be to repeat this experiment under fluorescence microscopy. Unfortunately, as hinted upon before, the camera did not seem to be sensitive enough for the available fluorescent particles at a reasonable frame rate.

4.4 Clustering Effect

In the course of the thesis work, the clustering became a major factor in the dynamic of the experiments. Therefore, the focus shifted more towards it and the information that can be drawn from it. We should note that the clustering did not happen, when no rod was present in the sample. It was mentioned in Chapter 2 that the primary forces that influence the system are of optical, thermal and fluidic nature. The aim of the clustering investigation is to try to get information on the latter from the clustering behaviour. In order to do this, I measured the brightness of a cluster that formed around an optically trapped rod and how it changes over time. This was done for linear and circular polarization, which yield a non-rotating and a rotating nanorod, respectively. The clustering was also measured at different laser powers, where a higher power means a faster rotation [40]. This way, we want to see the effects that the rotation itself, as well as different frequencies have on the clustering.

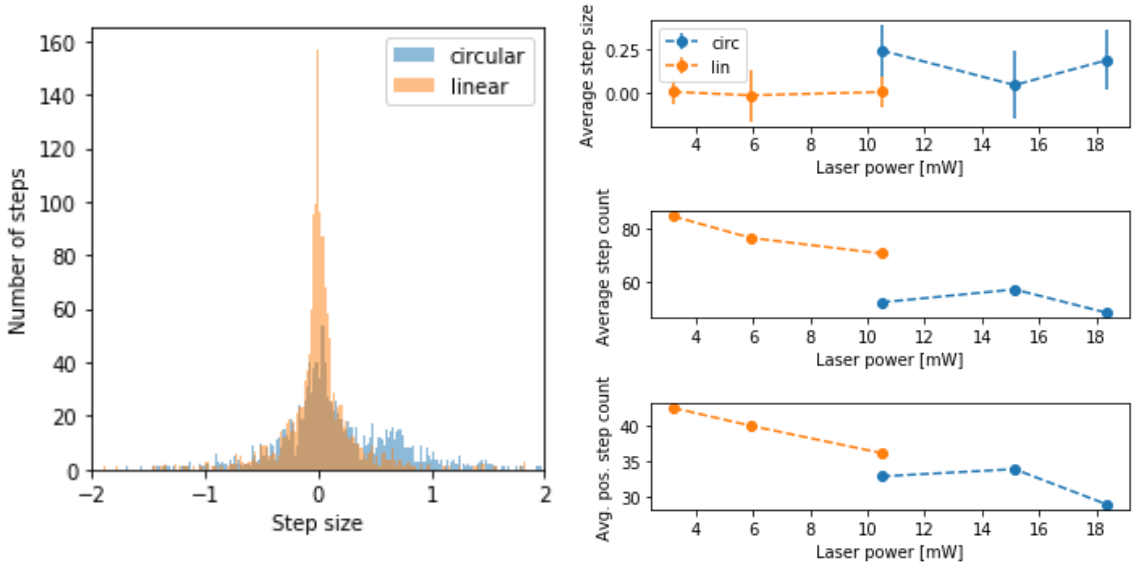

(a) (b)

Figure 4.3: Cluster growth measured as step-wise change in the cluster brightness. (a) A histogram of all recorded steps with linear and circular polarizations. The peaks centered around zero probably corresponds to noise, while the small second peak at circular polarization probably represents the average step size if a particle enters the cluster. The histograms show the steps of all measurements at all laser powers. (b) The average step size, as well as numbers of total steps and only positive steps for circular and linear polarizations at various laser powers.

4.4.1 Isolation of Steps

Figure 4.3a shows a histogram of all recorded steps for each of the two polarizations. Figure 4.3b compares the clustering behaviour between the two polarizations and different laser powers. It shows the average step size, the average amount of steps and the average amount of positive steps for these different conditions. We can see that the laser powers that are used for the two polarizations are different. This is due to the mistake in the laser power measurement that is described in Sections 3.2.1 and 4.1. While this makes it difficult to compare the two, it still seems like the average step size is constant at almost zero for linear polarization, while the amount of steps is higher than for circular polarization. This can be explained by the fact, that, as can be observed in Fig 4.3a, the zero-peak is much larger for linear polarization. This then gives a greater amount of small steps compared to circular polarization. The reason that so many steps around zero are recorded probably lies in the method of step detection, which is explained in Section 3.2.4. Since the determination of the threshold is up to the user and the clustering appears to be weaker, the y-axis will show a different scale during the detection process. This might get the user to interpret more noise as steps and thereby adjusting the threshold such that it includes more of these. Of course, there can not be a step with a step size of exactly zero, but the peak encapsulates very small steps that fall into this bin of the histogram.

The need to filter out the zero-peak is also supported by the histograms (a)-(c) in Figure 4.4. These show the step histograms at circular polarization for different laser powers. The idea is to use these in order to extract information on the influence of the laser power on the clustering. In order to do this, we want to fit the peaks of the histograms to compare them. However, due to the dominance of the zero-peak, it is not possible to fit the second peak in these individual histograms, even though it is clearly visible with the naked eye.

Due to this dominance of the zero-peak, this information does not yield any insight into the actual clustering behaviour. To gain a better access to the information in this data, we will try to take out the noise and focus on the actual steps. In Fig 4.3a, next to the large zero-peak, we can see a smaller peak to its right, which we assume contains the information on the majority of actual steps. We will therefore try to isolate these steps from the large zero-peak. Since this second peak is much more pronounced at circular polarization, we will focus on this for a bit in order to do this.

Figure 4.4d shows a histogram of all recorded steps at all laser powers at circular polarization. We can identify the two peaks, which are fitted as Gaussians of the

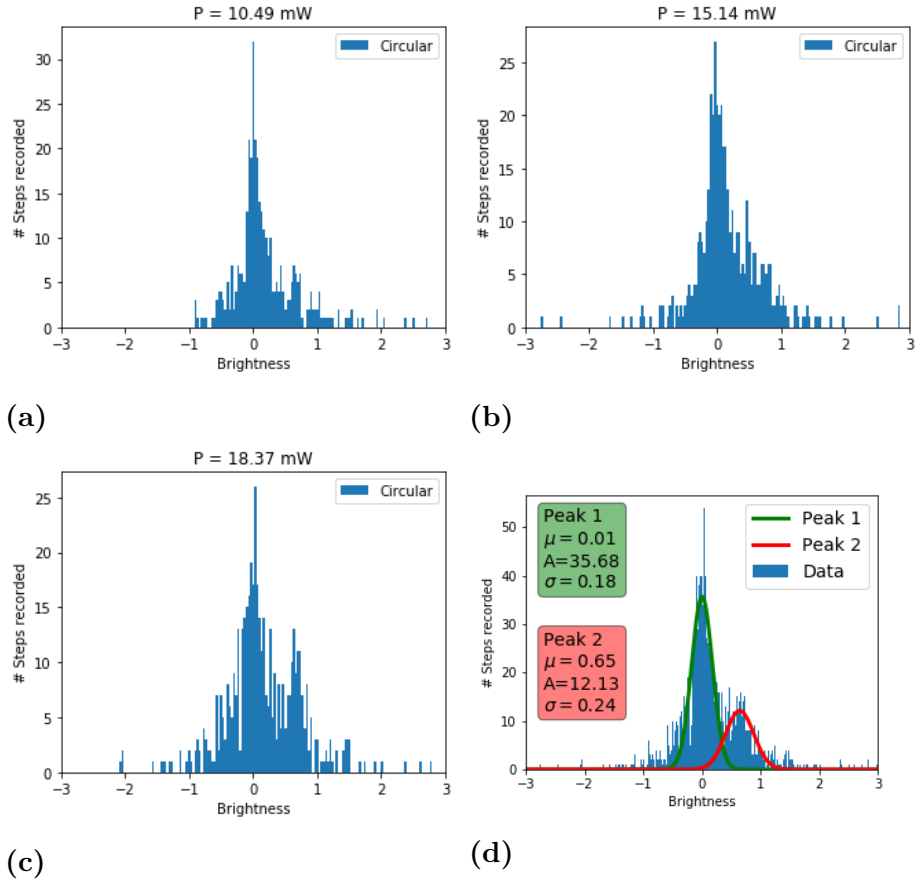

Figure 4.4: (a-c) Histograms showing all recorded steps at a given laser power for circular polarization. The title over each histogram refers to the applied laser power in mW. (d) Histogram of all recorded steps at circular polarization with its peaks fitted with a Gaussian function.

form

$$g = A \cdot \exp\left(\frac{-(x-\mu)^2}{2\sigma^2}\right) \quad . \tag{4.2}$$

The larger peak is around zero, meaning that these events probably correspond to noise and not particles moving into the cluster. The second, smaller one though is at around 0.65. We can draw the conclusion that this is the average change in brightness when one particle enters or leaves the cluster.

In order to isolate the steps from the noise, we will now cut out all incidents belonging to the zero-peak. Following the fitting values in Fig 4.4d, a minimum step size value of $|\mu - \sigma| = 0.65 - 0.24 = 0.41$ was chosen, following the fit in Figure 4.4d, where μ is the peak position in terms of brightness and σ is its width.

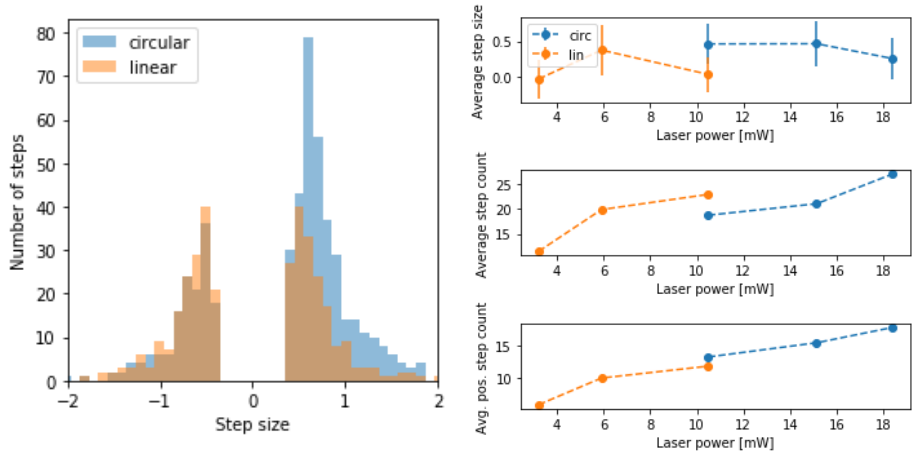

(a) (b)

Figure 4.5: (a) A plot of the average number of steps (center), the average number of positive steps (bottom) and the average size of the steps (top) for all used laser powers, using the filtered steps. (b) Histograms for all steps after filtering out the zero-peak, comparing circular (blue) and linear polarization (red).

4.4.2 Cluster Growth Dependence on Polarization and Laser Power

Fig 4.5 shows the new plots, acquired after applying this step filter described in the previous section. For comparison, Fig 4.3 show the previous plots without the filter once more. When comparing Figures 4.3a and 4.5a, we can see that the amount of steps is drastically reduced for linear polarization, as the majority of its steps fall in the filtered area. If we look at Fig 4.5b, we can now see that the curves of both the amount of steps overall and the amount of positive steps seem to follow similar behaviours for both polarizations. However, the amount of positive steps still appears to be slightly larger for circular polarization. This could indicate a dependence of the clustering on the rotation of the rod. More precisely, the rotation of the rod could correlate with the emergence and growth of a cluster. It also shows that the average step sizes between the polarizations are different as well, with the steps for linear polarization being on average lower than for circular. This can be explained by Fig 4.5a. There we can see that the amount of positive steps compared to the amount of negative steps is much higher for circular polarization, while it is almost the same for linear polarization, resulting in lower average values. However, we also have to consider here, that a higher laser power was applied when using circular polarization, meaning that this could also be an effect dependent on laser power, rather than polarization.

Figure 4.5b very clearly suggests that the clustering is also supported by an increase

in laser power, as both the amount of total steps and the amount of positive steps rise with it. We can investigate this a bit further by looking at histograms, showing the amount of steps for the different laser powers. We will refer to the ones recorded with circular polarization, as these showed a stronger clustering, possibly due to the higher power used here, and therefore provides more steps that can go into this. These histograms can be observed in Fig 4.6. Comparing the three histograms, we can see that there is a clear increase in the amplitude of the positive peak, indicating an increase in clustering following the laser power.

However, at the first two laser powers, the negative peaks stays roughly the same, while the third histogram shows a large increase of around 100 % in these negative steps. This could indicate that the cluster is generally becoming more dynamic with more particles moving in, but also more particles moving out. The reason for this might lie in the thermodynamic behaviour of the system: As the laser power increases, the rod is heating up. Potentially, thermophoresis comes into play. This means that the liquid close to the rod heats up with it, creating a temperature gradient through the liquid. As the molecules in the hotter areas have more kinetic energy due to the increased temperature, they push the particles away from the rod. With increasing laser power, this effect could become more prominent, influencing the system more and more. While it was not part of the measurement discussed here, it was qualitatively observed that the clusters become more unstable with increasing laser power, however this was not investigated in detail as time did unfortunately not allow for it.

4.4.3 Method assessment

Table 4.1 shows a table with the average discrepancies and the modelled curves at the various polarizations and laser powers. The values were determined as described in Section 3.2.4. For each dataset, the final value of the modelled curve is compared to the last value of the original data. The values presented in Table 4.1 describe the average for that particular laser power and the amount of dataset at the power is given.

Generally, for circular polarization, it is more convenient to use the percentage as comparison, as the cluster growth is large enough for a single step to have a smaller impact on the absolute brightness value. here, brightness values of up to 35 were reached, making the brightness value of a single step rather small in comparison. At linear polarization, however, the final brightness values rarely exceeded values around 8, meaning that one step carries more weight when using a relative measurement. This explains the rather large difference between the relative values at circular and linear polarization: The clustering seems to be weaker and more unsta-

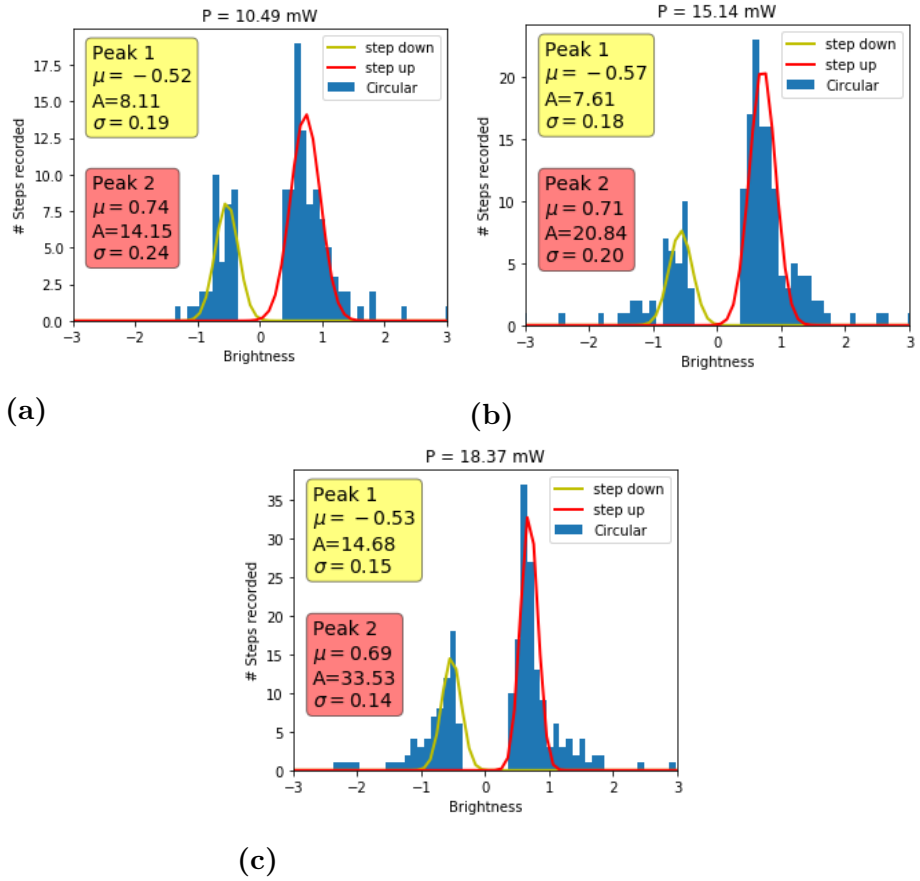

Figure 4.6: Histograms showing all recorded steps larger than 0.41 at a given laser power for circular polarization. The title over each histogram refers to the applied laser power in mW. The peaks are fitted following a Gaussian function.

ble for linear polarization, often yielding final values around 0. In this case, even a small difference from the recreated value means a large relative difference. A good example for this is the value at 10.55 mW, where the difference between the original and recreated value is 1254 % for all and 806 % for filtered steps, while the absolute differences are lower than all values at circular polarization.

The table suggests, that linear polarization yields more precise values in absolute terms. This is reasonable, since less cluster growth appears to happen here, meaning that less steps are detected and since each recorded step can contain an error, less of these play a role in the recreation of the curves. The comparably low values for the relative difference however show that the method is not completely arbitrary but still seems to give reasonable results.

When comparing the results for all detected steps and for the filtered steps, one can see that the former seems to be more precise for circular polarization, where

		All		Filtered		
Pol	LP [mW]	Diff	Diff%	Diff	Diff%	#
circ	10.49	1.77	0.12	3.07	0.25	7
	15.14	2.47	0.14	3.63	0.27	7
	18.37	1.64	0.16	1.86	0.21	8
lin	5.73	0.61	2.20	0.42	2.29	6
	8.14	1.07	0.73	1.33	0.83	6
	10.55	0.85	12.54	0.84	8.06	6

Table 4.1: A table showing the precision with which the original curves were recreated using the collected steps. LP refers to the laser power, *Diff* to the absolute difference between the last values of the model curve and the original curve, *Diff%* to the ratio of *Diff* and the original value and # gives the number of dataset for each laser power.

more steps are recorded. This might indicate that steps that are smaller than the set threshold for the filtering of the steps, do in fact not only result from noise but could also represent particles entering the cluster. One could imagine that not all particles contribute evenly to the brightness. For example, the light emitted from particles at the bottom of the clusters might be blocked by the particles above it. However, we want to investigate the general trend of the influence of polarization and laser power on the cluster growth and since the upcoming results seem to be quite clear, the method should still be able to give information on these issues.

5

Conclusion and Outlook

The results from Section 4.3 show that it is possible to directly track the trajectories of the particles in order to analyze flows around the nanorod. We can assume these trajectory investigations to yield reasonable results, as the diffusion analysis in 4.2 lead to realistic numbers. However, more sophisticated hardware, in the former of for example a faster and more sensitive camera or more suitable particles and light sources for fluorescence, would be needed for this. Furthermore, it would be advised to use thinner sample cells than used in this project. A good candidate for this would be cell number three, described in 3.1.2. Since the movement in vertical direction is minimized, this would lead to longer tracked trajectories and therefore more statistically significant results.

For further research, it would also be advantageous to use smaller and lighter tracer particles, in order to maximize the influence that a flow would have on them. Alternatively, methods not using tracer particles could be tried out, like using another optical tweezer for force measurement [54]. Removing tracer particles from the system has the advantage, that the clustering will not influence the measurement in the same way as discussed in this report.

For the analysis of the clustering, it is particularly unfortunate that the mistake in the laser power measurement (see Sections 3.2.1 and 4.1) was uncovered quite late in the process of this study. It made it very unclear if and how the polarization really influences the clustering behaviour of the tracer particles. It would be of interest to repeat the experiments with comparable laser powers. I will note that qualitatively, it seemed like circular polarization provides stronger clustering.

While this can not be validated clearly in this report, the amount of positive steps still seems to be higher for circular polarization, as seen in Figure 4.5b. This could indicate a stronger clustering with circularly polarized light, and therefore with a rotating nanorod. The experiments were all conducted under the same environmental circumstances, the only difference being the polarization of the trapping laser. At linear polarization, about twice as much of the absorbed laser power would be delivered to the rod compared to circular polarization at the same laser power, meaning

that we would have stronger thermophoretic forces in this case, which would counter the clustering. It is therefore not possible to conclude what the underlying force would that supports the clustering. It could either be some sort of fluidic effect from the rotating nanorod or the weaker thermophoretic forces that influence the particles around the rod at circularly polarized light.

A conclusion that can be drawn very clearly from the investigation of the clustering is, that the effect is more pronounced, the stronger the laser power. This is very clearly supported by Figure 4.5a and 4.5b. All indicators in these tend upwards with increased power. This observation is not very surprising, as a higher laser power also means an increase in the relevant forces, namely optical and fluidic effects.

To gain better insight into the nature of the clustering, the obvious next step would now of course be to repeat the clustering measurements with the right laser powers applied. However, after that, it would be of interest to explore the movement of the particles inside the cluster in order to deepen the understanding of the effects that appear in this system and explore possible applications inside the very active research field of nanoparticle assembly and structuring.

Bibliography

[1] A. Ashkin, "Acceleration and trapping of particles by radiation pressure", *Physical review letters*, vol. 24, no. 4, p. 156, 1970.

[2] A. Ashkin and J. Dziedzic, "Optical levitation by radiation pressure", *Applied Physics Letters*, vol. 19, no. 8, pp. 283–285, 1971.

[3] A. Ashkin, J. M. Dziedzic, J. Bjorkholm, and S. Chu, "Observation of a single-beam gradient force optical trap for dielectric particles", *Optics letters*, vol. 11, no. 5, pp. 288–290, 1986.

[4] P. Lebedew, "Untersuchungen über die druckkräfte des lichtes", *Annalen der Physik*, vol. 311, no. 11, pp. 433–458, 1901.

[5] E. F. Nichols and G. F. Hull, "The pressure due to radiation.(second paper.)", *Physical Review (Series I)*, vol. 17, no. 1, p. 26, 1903.

[6] O. M. Maragò, P. H. Jones, P. G. Gucciardi, G. Volpe, and A. C. Ferrari, "Optical trapping and manipulation of nanostructures", *Nature nanotechnology*, vol. 8, no. 11, p. 807, 2013.

[7] A.-I. Bunea and J. Glückstad, "Strategies for optical trapping in biological samples: Aiming at microrobotic surgeons", *Laser & Photonics Reviews*, vol. 13, no. 4, p. 1 800 227, 2019.

[8] Y. Yuan, Y. Lin, B. Gu, N. Panwar, S. C. Tjin, J. Song, J. Qu, and K.-T. Yong, "Optical trapping-assisted sers platform for chemical and biosensing applications: Design perspectives", *Coordination Chemistry Reviews*, vol. 339, pp. 138–152, 2017.

[9] M. L. Juan, M. Righini, and R. Quidant, "Plasmon nano-optical tweezers", *Nature photonics*, vol. 5, no. 6, p. 349, 2011.

[10] G. M. Burrow and T. K. Gaylord, "Multi-beam interference advances and applications: Nano-electronics, photonic crystals, metamaterials, subwavelength structures, optical trapping, and biomedical structures", *Micromachines*, vol. 2, no. 2, pp. 221–257, 2011.

[11] H. Yu, Y. Peng, Y. Yang, and Z.-Y. Li, "Plasmon-enhanced light–matter interactions and applications", *npj Computational Materials*, vol. 5, no. 1, pp. 1–14, 2019.

[12] L. Shao, Z.-J. Yang, D. Andren, P. Johansson, and M. Kall, "Gold nanorod rotary motors driven by resonant light scattering", *ACS nano*, vol. 9, no. 12, pp. 12 542–12 551, 2015.

[13] Y. E. Lee, K. H. Fung, D. Jin, and N. X. Fang, "Optical torque from enhanced scattering by multipolar plasmonic resonance", *Nanophotonics*, vol. 3, no. 6, pp. 343–350, 2014.

[14] L. Shao and M. Käll, "Light-driven rotation of plasmonic nanomotors", *Advanced Functional Materials*, vol. 28, no. 25, p. 1 706 272, 2018.

[15] M. Grzelczak, J. Vermant, E. M. Furst, and L. M. Liz-Marzán, "Directed self-assembly of nanoparticles", *ACS nano*, vol. 4, no. 7, pp. 3591–3605, 2010.

[16] Z. Nie, A. Petukhova, and E. Kumacheva, "Properties and emerging applications of self-assembled structures made from inorganic nanoparticles", *Nature nanotechnology*, vol. 5, no. 1, pp. 15–25, 2010.

[17] K. Thorkelsson, P. Bai, and T. Xu, "Self-assembly and applications of anisotropic nanomaterials: A review", *Nano Today*, vol. 10, no. 1, pp. 48–66, 2015.

[18] P. H. Jones, O. M. Maragò, and G. Volpe, *Optical tweezers: Principles and applications*. Cambridge University Press, 2015.

[19] M. Woerdemann, C. Alpmann, M. Esseling, and C. Denz, "Advanced optical trapping by complex beam shaping", *Laser & Photonics Reviews*, vol. 7, no. 6, pp. 839–854, 2013.

[20] C. Bradac, "Nanoscale optical trapping: A review", *Advanced Optical Materials*, vol. 6, no. 12, p. 1 800 005, 2018.

[21] A. S. Urban, S. Carretero-Palacios, A. A. Lutich, T. Lohmüller, J. Feldmann, and F. Jäckel, "Optical trapping and manipulation of plasmonic nanoparticles: Fundamentals, applications, and perspectives", *Nanoscale*, vol. 6, no. 9, pp. 4458–4474, 2014.

[22] S. A. Maier, *Plasmonics: fundamentals and applications*. Springer Science & Business Media, 2007.

[23] S. Enoch and N. Bonod, *Plasmonics: from basics to advanced topics*. Springer, 2012, vol. 167.

[24] C. Kittel, P. McEuen, and P. McEuen, *Introduction to solid state physics*. Wiley New York, 1996, vol. 8.

[25] P. Mulvaney, "Surface plasmon spectroscopy of nanosized metal particles", *Langmuir*, vol. 12, no. 3, pp. 788–800, 1996.

[26] E. Boulais, R. Lachaine, A. Hatef, and M. Meunier, "Plasmonics for pulsed-laser cell nanosurgery: Fundamentals and applications", *Journal of Photochemistry and Photobiology C: Photochemistry Reviews*, vol. 17, pp. 26–49, 2013.

[27] B. Špačková, P. Wrobel, M. Bocková, and J. Homola, "Optical biosensors based on plasmonic nanostructures: A review", *Proceedings of the IEEE*, vol. 104, no. 12, pp. 2380–2408, 2016.

[28] J. Mejıa-Salazar and O. N. Oliveira Jr, "Plasmonic biosensing: Focus review", *Chemical reviews*, vol. 118, no. 20, pp. 10 617–10 625, 2018.

[29] L. G. Devi and R. Kavitha, "A review on plasmonic metal tio2 composite for generation, trapping, storing and dynamic vectorial transfer of photogenerated electrons across the schottky junction in a photocatalytic system", *Applied surface science*, vol. 360, pp. 601–622, 2016.

[30] V. G. Kravets, A. V. Kabashin, W. L. Barnes, and A. N. Grigorenko, "Plasmonic surface lattice resonances: A review of properties and applications", *Chemical reviews*, vol. 118, no. 12, pp. 5912–5951, 2018.

[31] K. Ueno, V. Mizeikis, S. Juodkazis, K. Sasaki, and H. Misawa, "Optical properties of nanoengineered gold blocks", *Optics letters*, vol. 30, no. 16, pp. 2158–2160, 2005.

[32] K. C. Neuman and S. M. Block, "Optical trapping", *Review of scientific instruments*, vol. 75, no. 9, pp. 2787–2809, 2004.

[33] R. Loudon and S. M. Barnett, "Theory of the radiation pressure on dielectric slabs, prisms and single surfaces", *Optics Express*, vol. 14, no. 24, pp. 11 855–11 869, 2006.

[34] H. Šípová-Jungová, D. Andrén, S. Jones, and M. Käll, "Nanoscale inorganic motors driven by light: Principles, realizations, and opportunities", *Chemical Reviews*, vol. 120, no. 1, pp. 269–287, 2019.

[35] A. Lehmuskero, R. Ogier, T. Gschneidtner, P. Johansson, and M. Käll, "Ultrafast spinning of gold nanoparticles in water using circularly polarized light", *Nano letters*, vol. 13, no. 7, pp. 3129–3134, 2013.

[36] T. A. Nieminen, A. B. Stilgoe, N. R. Heckenberg, and H. Rubinsztein-Dunlop, "Angular momentum of a strongly focused gaussian beam", *Journal of Optics A: Pure and Applied Optics*, vol. 10, no. 11, p. 115 005, 2008.

[37] S. H. Simpson and S. Hanna, "Optical angular momentum transfer by laguerre-gaussian beams", *JOSA A*, vol. 26, no. 3, pp. 625–638, 2009.

[38] R. A. Beth, "Mechanical detection and measurement of the angular momentum of light", *Physical Review*, vol. 50, no. 2, p. 115, 1936.

[39] M. Friese, T. Nieminen, N. Heckenberg, and H. Rubinsztein-Dunlop, "Optical alignment and spinning of laser-trapped microscopic particles", *Nature*, vol. 394, no. 6691, pp. 348–350, 1998.

[40] H. Šípova, L. Shao, N. Odebo Länk, D. Andrén, and M. Käll, "Photothermal dna release from laser-tweezed individual gold nanomotors driven by photon angular momentum", *ACS Photonics*, vol. 5, no. 6, pp. 2168–2175, 2018.

[41] A. Einstein, "Über die von der molekularkinetischen theorie der wärme geforderte bewegung von in ruhenden flüssigkeiten suspendierten teilchen", *Annalen der physik*, vol. 4, 1905.

[42] H. A. Lorentz, *Abhandlungen über theoretische Physik*. BG Teubner, 1907.

[43] Z. Zhang and C.-H. Menq, "Three-dimensional particle tracking with subnanometer resolution using off-focus images", *Applied optics*, vol. 47, no. 13, pp. 2361–2370, 2008.

[44] ThermoFisherScientific. (Sep. 2020). Fluospheres™ carboxylate-modified microspheres, 0.1 µm, red fluorescent (580/605), 2% solids, [Online]. Available: `https://www.thermofisher.com/order/catalog/product/F8801#/F8801`.

[45] U. Böhm, S. W. Hell, and R. Schmidt, "4pi-resolft nanoscopy", *Nature communications*, vol. 7, no. 1, pp. 1–8, 2016.

[46] P. Rudquist, D. Elfström, S. T. Lagerwall, and R. Dabrowski, "Polymer-stabilized orthoconic antiferroelectric liquid crystals", *Ferroelectrics*, vol. 344, no. 1, pp. 177–188, 2006.

[47] M. Czerwiński, M. Urbańska, N. Bennis, and P. Rudquist, "Influence of the type of phase sequence and polymer-stabilization on the physicochemical and electro-optical properties of novel high-tilt antiferroelectric liquid crystalline materials", *Journal of Molecular Liquids*, vol. 288, p. 111 057, 2019.

[48] M. Hertzog, P. Rudquist, J. A. Hutchison, J. George, T. W. Ebbesen, and K. Börjesson, "Voltage-controlled switching of strong light–matter interactions using liquid crystals", *Chemistry–A European Journal*, vol. 23, no. 72, pp. 18 166–18 170, 2017.

[49] S. H. Gage, "Modern dark-field microscopy and the history of its development", *Transactions of the American Microscopical Society*, vol. 39, no. 2, pp. 95–141, 1920.

[50] J. W. Lichtman and J.-A. Conchello, "Fluorescence microscopy", *Nature methods*, vol. 2, no. 12, pp. 910–919, 2005.

[51] C. T. Rueden, J. Schindelin, M. C. Hiner, B. E. DeZonia, A. E. Walter, E. T. Arena, and K. W. Eliceiri, "Imagej2: Imagej for the next generation of scientific image data", *BMC bioinformatics*, vol. 18, no. 1, p. 529, 2017.

[52] J. Schindelin, I. Arganda-Carreras, E. Frise, V. Kaynig, M. Longair, T. Pietzsch, S. Preibisch, C. Rueden, S. Saalfeld, B. Schmid, *et al.*, "Fiji: An open-source platform for biological-image analysis", *Nature methods*, vol. 9, no. 7, pp. 676–682, 2012.

[53] R. W. Schafer, "What is a savitzky-golay filter?[lecture notes]", *IEEE Signal processing magazine*, vol. 28, no. 4, pp. 111–117, 2011.

[54] H. Mushfique, J. Leach, H. Yin, R. D. Leonardo, M. J. Padgett, and J. M. Cooper, "3d mapping of microfluidic flow in laboratory-on-a-chip structures using optical tweezers", *Analytical chemistry*, vol. 80, no. 11, pp. 4237–4240, 2008.